Inorganic Chemistry

pubs.acs.org/IC Article

Capped Nanojars: Synthesis, Solution and Solid-State Characterization, and Atmospheric CO_2 Sequestration by Selective Binding of Carbonate

Wisam A. Al Isawi, Matthias Zeller, and Gellert Mezei*

Cite This: *Inorg. Chem.* 2021, 60, 13479−13492 Read Online

ACCESS | Metrics & More | Article Recommendations | Supporting Information

ABSTRACT: Nanojars are a class of supramolecular anion-incarcerating coordination complexes that self-assemble from Cu^{2+} ions, pyrazole, and a strong base in the presence of highly hydrophilic anions. In this work, we show that if the strong base (e.g., NaOH or Bu_4NOH) is replaced by a weak base such as a trialkylamine, capped nanojars of the formula $[\{Cu_3(\mu_3\text{-OH})(\mu\text{-pz})_3L_3\}CO_3\subset\{Cu(\mu\text{-OH})(\mu\text{-pz})\}_n]$ (pz = pyrazolate anion; L = neutral donor molecule; n = 27−31) are obtained instead of the conventional nanojars. Yet, to obtain capped nanojars, the conjugate acid side product originating from the weak base must be separated by transferring it to water either by precipitation of the water-insoluble capped nanojars or by liquid−liquid extraction. Full characterization using electrospray ionization mass spectrometry, UV−vis and variable-temperature ^1H NMR spectroscopy in solution, and single-crystal X-ray diffraction, elemental analysis, and solubility studies in the solid state reveals similarities as well as drastic differences between capped nanojars and nanojars lacking the $[Cu_3(\mu_3\text{-OH})(\mu\text{-pz})_3L_3]^{2+}$ cap. Acid−base reactivity studies demonstrate that capped nanojars are intermediates in the pH-controlled assembly−disassembly of nanojars. During the self-assembly of capped nanojars, CO_2 is selectively sequestered from air in the presence of other atmospheric gases and converted to carbonate, the binding of which is selective in the presence of NO_3^-, ClO_4^-, BF_4^-, Cl^-, and Br^- ions.

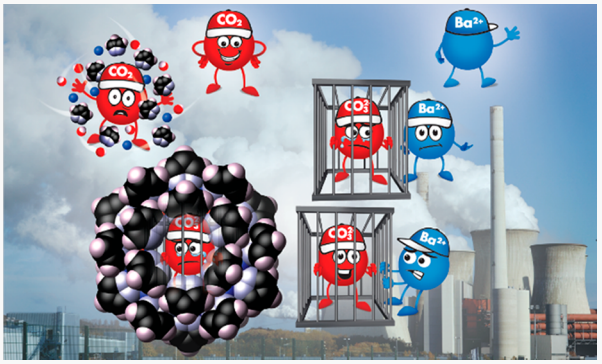

INTRODUCTION

Polynuclear copper(II) complexes have been extensively studied in the past few decades driven by their interesting spectroscopic, redox, and magnetic properties,[1−6] catalytic applications,[7−10] CO_2 fixation,[11−16] and relevance to multicopper enzymes.[17] The pyrazolate anion (pz, $C_3H_3N_2^-$) is particularly suitable for the construction of cyclic trinuclear and higher-nuclearity metal complexes, forming a wide variety of molecular architectures with copper or other metals (Figure 1). By far the most common copper(II) pyrazolate constructs are trinuclear, based on the $[Cu_3(\mu_3\text{-X})(\mu\text{-pz})_3L_3]$ moiety, where X is O^{2-}, OH^-, Cl^-, Br^-, or OMe^- and L is either a charged ligand, such as Cl^-, Br^-, N_3^-, NCO^-, NCS^-, OH^-, NO_3^-, NO_2^-, SO_4^{2-}, RPO_3^{2-}, $ROPO_3^{2-}$, carboxylates, and pyrazolate or a neutral species, such as water, pyrazole, pyridine, *N*,*N*-dimethylformamide (DMF), tetrahydrofuran (THF), or acetonitrile (CH_3CN).[18] Trinuclear units can be assembled into discrete hexanuclear units if L is a bridging ligand, such as pyrazolate,[19−24] NCS^-,[25] or 4,4′-bipyridine,[26] or if L or additional coordinating species, such as Cl,[27,28] carboxylates,[29−32] sulfate,[33,34] perchlorate,[35,36] or nitrate,[37] act as bridging ligands by binding to the axial position of one or multiple Cu^{II} ions. If L is a di- or tricarboxylate ligand or 4,4′-bipyridine (or its derivatives), then metal−organic frameworks[38−48] or coordination polymers[49−60] can be obtained. Various discrete higher-nuclearity copper(II) pyrazolate complexes are also known.[61−74]

A relatively newer addition to the realm of polynuclear copper(II) pyrazolate complexes is a family of large supramolecular assemblies, termed *nanojars*,[75] based on three or four $[cis\text{-}Cu^{II}(\mu\text{-OH})(\mu\text{-pz})]_m$ metallamacrocycles (m = 6−14, except 11). Nanojars of the formula $[anion\subset\{Cu^{II}(\mu\text{-OH})(\mu\text{-pz})\}_n]$ (**Cu$_n$**; n = 26−33) form from Cu^{2+}, OH^-, and pyrazolate ions only in the presence of small, highly hydrophilic anions, which template their formation. Once self-assembled, the nanojar wraps around the incarcerated anion using a multitude of hydrogen bonds and completely isolates it from the surrounding medium. Consequently, the anion (carbonate,[76] sulfate,[75−77] phosphate,[78] and arsenate[78]) is bound extremely strongly, so that an aqueous Ba^{2+} solution is unable to precipitate the corresponding highly insoluble

Received: June 17, 2021
Published: August 27, 2021

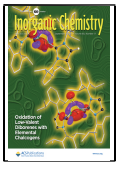

https://doi.org/10.1021/acs.inorgchem.1c01826
Inorg. Chem. 2021, 60, 13479−13492

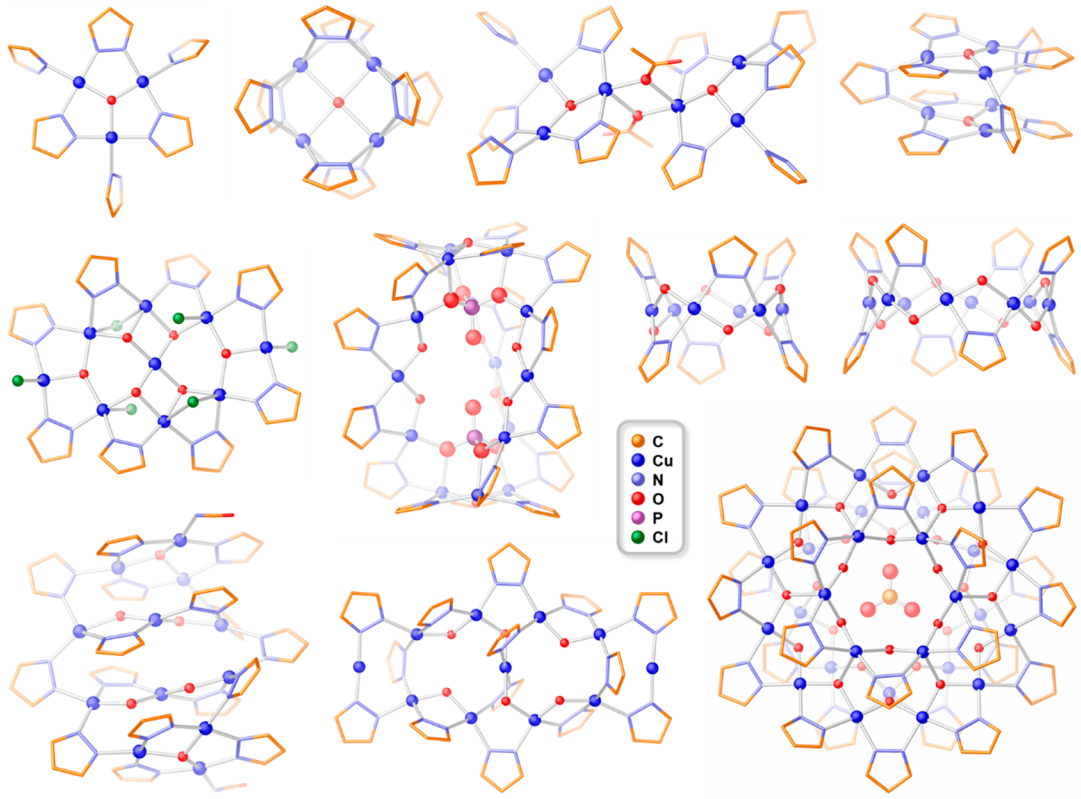

Figure 1. Examples of discrete coordination motifs formed by pyrazole (unsubstituted or with hydrocarbon/halogen substituents, which are omitted for clarity) with three or more Cu^{2+} ions.

barium salt (e.g., $BaSO_4$; $K_{sp} = 1.08 \times 10^{-10}$) when stirred with a solution of the nanojars. Owing to this exceptionally strong binding affinity, nanojars are able to transfer even the most hydrophilic anions, such as carbonate, from water into aliphatic solvents[79] and have been developed into extraction agents for the removal of such anions from contaminated aqueous media by liquid–liquid extraction.[80] The recognition and binding of anions is an important current field of research[81−83] because the supramolecular binding of anions finds applications in anion sensing, extraction and separation of anions, transmembrane anion transport, and anion-driven architectonics and organocatalysis.[84]

Although these peculiar yet fascinating complexes were discovered 2 decades ago,[85] progress in their development has been hindered by the difficulty of their characterization. Nanojars always form as a mixture of different sizes (such as **Cu_{27}-Cu_{31}** with carbonate or **Cu_{27}-Cu_{33}** with sulfate), which are impossible to separate individually using conventional separation techniques. Nanojars are highly soluble in most organic solvents, leaving few options for the growth of high-quality single crystals. Also, their large size/charge ratio hampered initial mass spectrometric studies, and the paramagnetic Cu^{2+} ions complicated initial NMR studies. Nevertheless, over the years, specific conditions have been established that have allowed for single-crystal growth and structural characterization of a few different nanojar species, as well as high-resolution mass spectrometric and ^1H NMR studies. These investigations have shed light on several aspects of nanojar chemistry, including the chemical etching of a nanojar mixture, leading to a single size of nanojar,[76] as well as the mechanism of nanojar formation.[86]

Here we describe a new class of *neutral* nanojars of the formula $[\{Cu_3(\mu_3\text{-OH})(\mu\text{-pz})_3L_3\}CO_3\subset\{Cu(\mu\text{-OH})(\mu\text{-pz})\}_n]$ (**Cu_3-Cu_n**), where L is a neutral donor ligand, such as water or the reaction solvent. As opposed to the 2− charged parent nanojars $[CO_3\subset\{Cu(\mu\text{-OH})(\mu\text{-pz})\}_n]^{2-}$ (**Cu_n**), which are charge-balanced by two Bu_4N^+ counterions, the former have an additional $[Cu_3(\mu_3\text{-OH})(\mu\text{-pz})_3L_3]^{2+}$ (**Cu_3**) "cap"; hence, they are termed *capped nanojars*.[78] These capped nanojars, which turn out to be a new intermediate in the formation of nanojars, have been characterized by electrospray ionization mass spectrometry (ESI-MS), UV–vis and variable-temperature ^1H NMR spectroscopy in solution, and single-crystal X-ray diffraction (in the case of **Cu_3-Cu_{27}**), elemental analysis, and solubility studies in the solid state. It is also shown that atmospheric CO_2 is selectively sequestered and incorporated as CO_3^{2-} during their self-assembly. Because of the current threat of global warming, the development of novel methods for the removal of CO_2 from Earth's atmosphere is an urgent endeavor.[87]

RESULTS AND DISCUSSION

Synthesis and Mass Spectrometric Studies. Nanojars are usually prepared according to the reaction illustrated by eq 1.

$$n\mathrm{Cu(NO_3)_2\cdot 2.5H_2O} + n\mathrm{Hpz} + 2(n-1)\mathrm{NaOH} + 2\mathrm{Bu_4NOH} + \mathrm{Na_2CO_3} \xrightarrow{\mathrm{THF}} (\mathrm{Bu_4N})_2[\mathrm{CO_3}\{\mathrm{Cu}(\mu\text{-OH})(\mu\text{-pz})\}_n] + 2n\mathrm{NaNO_3} + 3.5n\mathrm{H_2O} \quad (1)$$

https://doi.org/10.1021/acs.inorgchem.1c01826
Inorg. Chem. 2021, 60, 13479−13492

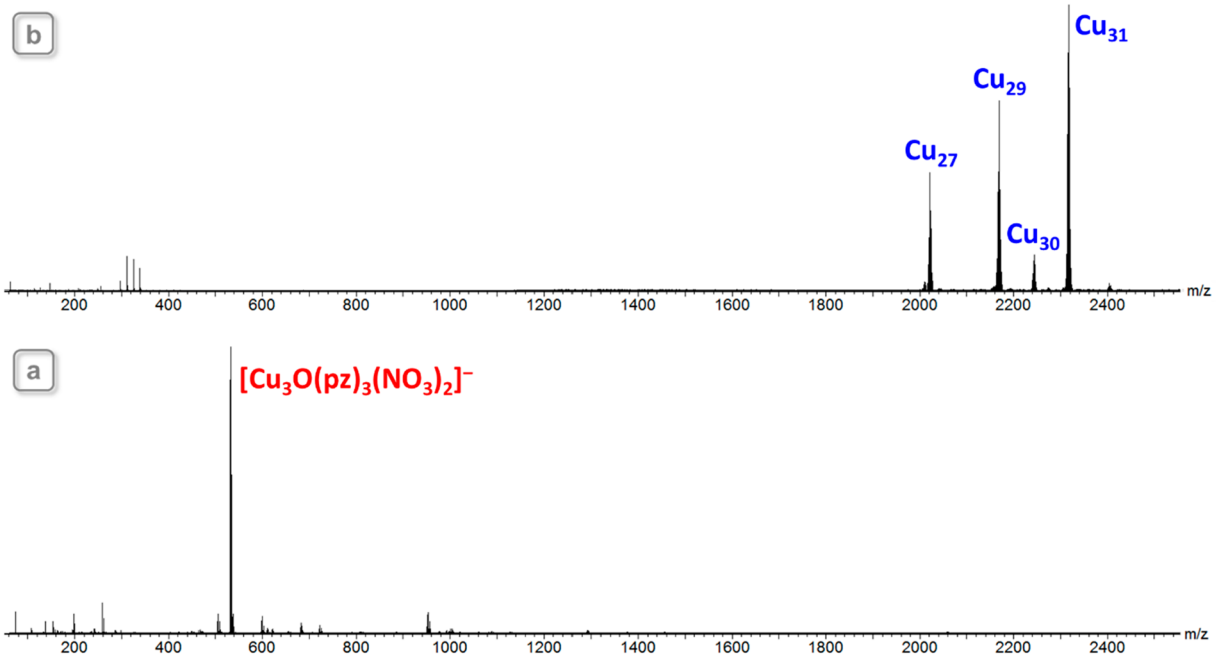

Figure 2. ESI-MS spectra in CH_3CN of (a) the solution of $Cu(NO_3)_2{\cdot}2.5H_2O$, pyrazole, and Et_3N (1:1:2 molar ratio in THF) and (b) the solid that precipitates upon pouring the solution into excess water.

Because NaOH is not soluble in THF (or other organic solvents suitable for the synthesis of nanojars) and the reactions usually need 2−3 days for completion, a base soluble in organic solvents was sought instead of NaOH. Bu_4NOH is a good alternative, but it is expensive to use on a large scale. Triethylamine (Et_3N), which is commonly used in coordination chemistry for deprotonation purposes, was chosen as an inexpensive base soluble in organic solvents. When $Cu(NO_3)_2{\cdot}2.5H_2O$, pyrazole, and Et_3N (1:1:2 molar ratio) are mixed in THF, a clear, deep-blue solution is obtained. ESI-MS(−) of this solution indicates a major peak at m/z 532 corresponding to $[Cu_3O(pz)_3(NO_3)_2]^-$, which suggests the formation of $Et_3NH[Cu_3(OH)(pz)_3(NO_3)_3]$ (Figure 2a). The spectrum also shows the complete absence of nanojars in the m/z 2000−2400 region. When this solution is poured into excess water, however, a dark-blue solid precipitates and a colorless filtrate is obtained. The ESI-MS(−) spectrum of the solid suggests the formation of $[CO_3{\subset}\{Cu(\mu\text{-}OH)(\mu\text{-}pz)\}_n]^{2-}$ nanojars (**Cu$_n$**; n = 27, m/z 2023; n = 29, m/z 2171; n = 30, m/z 2245; n = 31, m/z 2318) and shows the absence of smaller-nuclearity complexes (Figure 2b). Earlier it was assumed that the counterions of these nanojars were Et_3NH^+,[75] which form upon deprotonation of water and pyrazole by Et_3N to provide OH^- and pz^- ions needed for the formation of the nanojars ($Et_3N + H_2O \rightarrow Et_3NH^+ + HO^-$). Later, however, it was shown that nanojars decompose in the presence of acids, even very weak ones, such as $Mg^{2+}(aq)$ and $Ca^{2+}(aq)$, with pK_a values of 11.2 and 12.7, respectively.[86] Therefore, nanojars are not expected to be stable in the presence of Et_3NH^+, which has a pK_a of 10.75, a presumption supported by the absence of nanojar peaks in the ESI-MS(−) spectrum of the THF solution of $Cu(NO_3)_2{\cdot}2.5H_2O$, pyrazole, and Et_3N. Yet, the solid product that precipitates out of water is stable in contact with the aqueous solution of Et_3NH^+, which is acidic. It is now clear, as demonstrated by an array of different techniques described in the following sections, that the product obtained when Et_3N is employed for nanojar formation is not $(Et_3NH)_2[CO_3{\subset}\{Cu(\mu\text{-}OH)(\mu\text{-}pz)\}_n]$ but $[\{Cu_3(\mu_3\text{-}OH)(\mu\text{-}pz)_3L_3\}CO_3{\subset}\{Cu(\mu\text{-}OH)(\mu\text{-}pz)\}_n]$.

Instead of precipitation in water, capped nanojars can alternatively be prepared in an organic solvent immiscible with water, by liquid−liquid extraction of the triethylammonium nitrate byproduct. Thus, a solution of $Cu(NO_3)_2{\cdot}2.5H_2O$, pyrazole, and Et_3N (1:1:2 molar ratio) in benzonitrile, stirred with an equal volume of water for 5 min, provided a **Cu$_3$-Cu$_n$** mixture (Figure S1) similar to that obtained in THF and precipitated from water. Equation 2 describes the formation of capped nanojars.

$$\begin{aligned}&(n+3)Cu(NO_3)_2{\cdot}2.5H_2O + (n+3)Hpz \\ &\quad + 2(n+3)Et_3N + CO_2 \\ &\rightarrow [\{Cu_3(\mu_3\text{-}OH)(\mu\text{-}pz)_3L_3\}CO_3\{Cu(\mu\text{-}OH)(\mu\text{-}pz)\}_n] \\ &\quad + 2(n+3)Et_3NHNO_3 + (1.5n+5.5)H_2O \end{aligned} \quad (2)$$

It should be noted that the peaks of the neutral $[\{Cu_3(\mu_3\text{-}OH)(\mu\text{-}pz)_3L_3\}CO_3{\subset}\{Cu(\mu\text{-}OH)(\mu\text{-}pz)\}_n]$ cannot be expected in the mass spectrum. It is apparent that, during ionization in the mass spectrometer, the $[Cu_3(\mu_3\text{-}OH)(\mu\text{-}pz)_3L_3]^{2+}$ "cap" detaches from the neutral capped nanojars, which then become observable as $[CO_3{\subset}\{Cu(\mu\text{-}OH)(\mu\text{-}pz)\}_n]^{2-}$. This makes the differentiation between nanojars and capped nanojars by ESI-MS(−) alone impossible. As shown in Figures S2 and S3, the negative-mode in-source fragmentation patterns of **Cu$_3$-Cu$_n$** and **Cu$_n$** are also practically identical. However, the corresponding positive-mode patterns are distinct (Figures S4 and S5). The "cap" is clearly observed in the ESI-MS(+) spectrum of **Cu$_3$-Cu$_n$**, as is evidenced by a peak at m/z 408 corresponding to $[Cu_3O(pz)_3]^+$. This peak is absent in the ESI-MS(+) spectrum of **Cu$_n$**, which shows a peak for Bu_4N^+ instead (m/z 242).

https://doi.org/10.1021/acs.inorgchem.1c01826
Inorg. Chem. 2021, 60, 13479−13492

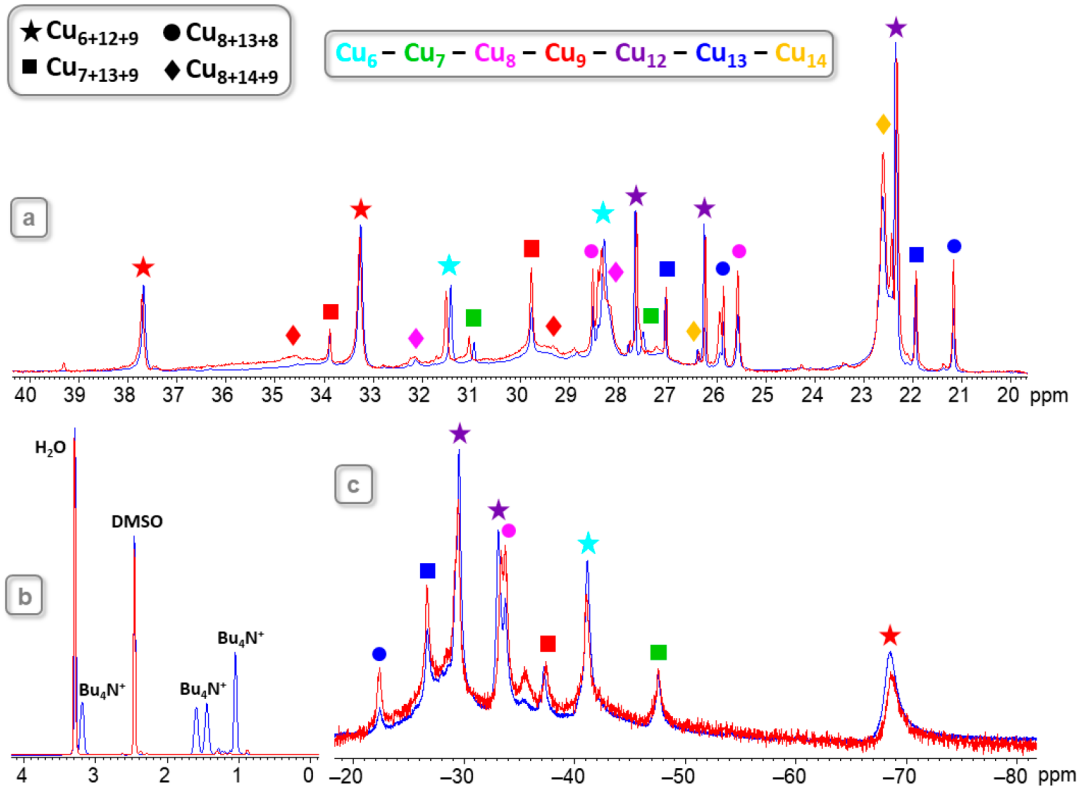

Figure 3. ^{1}H NMR spectra in DMSO-d_6 of **Cu$_3$-Cu$_n$** (red trace) and **Cu$_n$** (blue trace), showing regions for pyrazolate (a), counterion (b), and hydroxide (c) protons.

A puzzling observation was encountered when $(Bu_4N)_2[CO_3\subset\{Cu(\mu\text{-}OH)(\mu\text{-}pz)\}_{27}]$ (**Cu$_{27}$**), obtained by etching the $(Bu_4N)_2[CO_3\subset\{Cu(\mu\text{-}OH)(\mu\text{-}pz)\}_n]$ (n = 27, 29, 30, and 31) mixture with NH_3,[76] was purified by recrystallization from toluene by hexane vapor diffusion. To obtain a high-purity sample, the crystals were redissolved in toluene for a second recrystallization. Filtration of the toluene solution left behind a small amount of a dark-blue solid, which proved insoluble in pure toluene. When tested by ESI-MS(−) in a CH_3CN solution, this toluene-insoluble fraction provided a spectrum identical with that of toluene-soluble **Cu$_{27}$**. Further solubility testing showed that the as-synthesized toluene-insoluble **Cu$_3$-Cu$_n$** mixture is also vastly less soluble in other organic solvents (THF, ∼0.450 g/L; CH_3CN, ∼0.150 g/L) compared to **Cu$_n$** (THF, >70 g/L). Supported by the fact that NH_4^+ cannot serve as a counterion for nanojars because of its acidity (pK_a = 9.25), a closer analysis of the NH_3-etching reaction explains formation of the toluene-insoluble fraction, composed of capped nanojars. Regardless of their size, each **Cu$_n$** nanojar requires two Bu_4N^+ counterions for charge-neutrality (in other words, the molar ratio between any **Cu$_n$** nanojar and Bu_4N^+ is 1:2). Yet, on a mass basis, a smaller nanojar needs more Bu_4N^+ than a larger nanojar. For example, when $(Bu_4N)_2[CO_3\subset\{Cu(\mu\text{-}OH)(\mu\text{-}pz)\}_{31}]$ breaks down into $(Bu_4N)_2[CO_3\subset\{Cu(\mu\text{-}OH)(\mu\text{-}pz)\}_{27}]$, four $\{Cu(\mu\text{-}OH)(\mu\text{-}pz)\}$ moieties are left over. These will coalesce to form new nanojar units. However, in the absence of additional Bu_4N^+ counterions, capped nanojars also form (eq 3). These new species also need additional CO_3^{2-} ions, which could easily form from atmospheric CO_2 by reacting with OH^- groups originating from NH_3 ($NH_3 + H_2O \rightarrow NH_4^+ + HO^-$; $CO_2 + 2HO^- \rightarrow CO_3^{2-} + H_2O$). This hypothesis was tested by carrying out the NH_3-etching process in the presence of additional Bu_4NOH, as described by eq 4. No toluene-insoluble fraction was obtained in this case.

$$\frac{30}{n-27}(Bu_4N)_2[CO_3\{Cu(\mu\text{-}OH)(\mu\text{-}pz)\}_n] + CO_2 \xrightarrow{NH_3} \frac{30}{n-27}(Bu_4N)_2[CO_3\{Cu(\mu\text{-}OH)(\mu\text{-}pz)\}_{27}] + [\{Cu_3(\mu_3\text{-}OH)(\mu\text{-}pz)_3L_3\}CO_3\{Cu(\mu\text{-}OH)(\mu\text{-}pz)\}_{27}] + H_2O \quad (3)$$

$$27(Bu_4N)_2[CO_3\{Cu(\mu\text{-}OH)(\mu\text{-}pz)\}_n] + 2(n-27)Bu_4NOH + (n-27)CO_2 \xrightarrow{NH_3} n(Bu_4N)_2[CO_3\{Cu(\mu\text{-}OH)(\mu\text{-}pz)\}_{27}] + (n-27)H_2O \quad (4)$$

To test whether capped nanojars behave analogously to nanojars in the presence of NH_3, a solution of **Cu$_3$-Cu$_n$** in THF was saturated with gaseous NH_3 at room temperature. Standing for 12 days resulted in no visual changes. ESI-MS(−), however, shows the disappearance of the peaks at m/z 2171, 2245, and 2318 and displays only one major peak at m/z 2023 (Figure S6), indicating the conversion of **Cu$_3$-Cu$_{29}$**, **Cu$_3$-Cu$_{30}$**, and **Cu$_3$-Cu$_{31}$** to **Cu$_3$-Cu$_{27}$**, similarly to the conversion of **Cu$_{29}$**, **Cu$_{30}$**, and **Cu$_{31}$** to **Cu$_{27}$** observed earlier.[76]

^{1}H NMR Spectroscopy. The ^{1}H NMR spectrum of as-synthesized **Cu$_3$-Cu$_n$**, similarly to that of **Cu$_n$**,[76] is rather complex because it contains five to six overlapping sets of paramagnetically shifted peaks in the 21−38 ppm window, corresponding to Cu_{6+12+9}, Cu_{7+13+9}, Cu_{8+13+8}, Cu_{30} (Cu_{8+13+9}

https://doi.org/10.1021/acs.inorgchem.1c01826
Inorg. Chem. 2021, 60, 13479−13492

and/or Cu_{8+14+8}), and Cu_{8+14+9}. Within each Cu_m ring, all pyrazole and OH groups are magnetically identical, respectively, with the exception of the central rings with two different side rings, which show two sets of signals. The pyrazole units have two magnetically distinct sets of protons, one at the 4 position and one at the 3 and 5 positions (with 1:2 integrated intensities). As shown in Figure 3, the regions of the ^{1}H NMR spectra of **Cu_3-Cu_n** and **Cu_n** corresponding to pz^- protons (21−38 ppm) and HO^- protons (−20 to −70 ppm) are almost superimposable. Peaks corresponding to the $[Cu_3(\mu_3\text{−}OH)(\mu\text{-}pz)_3L_3]^{2+}$ "cap" of **Cu_3-Cu_n** could not be assigned unambiguously based on this spectrum alone, but they do show up at 37.2 ppm (4-*H*-pz) and 22.2 ppm (3,5-*H*-pz) upon treatment of the solution with gaseous NH_3 (see below). For comparison, the ^{1}H NMR signals of the pz^- protons of $[Cu_3(OH)(pz)_3(NO_3)_2(H_2O)]$[86] appear at 40.08 and 33.63 ppm in DMSO-d_6. The region between 0 and 4 ppm is clearly distinct because it shows the absence of Et_3NH^+ in the case of **Cu_3-Cu_n**, whereas peaks corresponding to the Bu_4N^+ counterions are present in the case of **Cu_n**.

Variable-temperature ^{1}H NMR studies show that **Cu_3-Cu_n** behaves differently from **Cu_n** upon heating in DMSO-d_6, with some similarities. In both cases, the **Cu_{7+13+9}** and **Cu_{8+14+9}** nanojars/capped nanojars convert to other sizes upon heating, and **Cu_{8+13+8}** appears to be the most stable species. However, while both **Cu_{6+12+9}** and **Cu_{8+13+8}** are still present after heating a nanojar mixture to 150 °C, only **Cu_{8+13+8}** is observed as major species at ∼70 °C in the case of capped nanojars. Above 70 °C, the **Cu_{8+13+8}** capped nanojar decomposes, giving rise to new, hitherto unidentified species (Figure 4).

To deduce details about the process of NH_3 etching of nanojars and capped nanojars, solutions of **Cu_n** and **Cu_3-Cu_n** in DMSO-d_6 were saturated with gaseous NH_3 and were monitored periodically by ^{1}H NMR (Figures 5 and S7). The signal of bulk NH_3 appears at 0.24 ppm right after bubbling it in the solution of **Cu_3-Cu_n** in DMSO-d_6, and over time it gradually shifts to −0.16 ppm after 7 days (0.35−0.18 ppm in the case of **Cu_n**). Immediately after NH_3 treatment, the disappearance of the **Cu_{7+13+9}** and **Cu_{8+14+9}** nanojars/capped nanojars is observed, accompanied by a marked increase in the signal intensity of the **Cu_{8+13+8}** species. Over time, a gradual transformation of **Cu_{8+13+8}** to **Cu_{6+12+9}** is observed. However, the conversion to **Cu_{6+12+9}** is not complete after 12 days (as is the case when THF was used as the solvent, as confirmed by ESI-MS in CH_3CN), even after a second saturation of the solution with fresh NH_3 after the first 7 days. Apparently, an equilibrium mixture of **Cu_{6+12+9}** and **Cu_{8+13+8}** is obtained (favoring the former), where two competing reactions take place: NH_3 is pushing the equilibrium toward forming more **Cu_{6+12+9}**, whereas DMSO-d_6 is converting **Cu_{6+12+9}** to **Cu_{8+13+8}**. Further proof for this is provided by the ESI-MS(−) spectrum of pure **Cu_3-Cu_{27}** (obtained by NH_3 etching of **Cu_3-Cu_n** in THF) dissolved in DMSO-d_6, which shows species with n = 27 and 29 instead of only **Cu_3-Cu_{27}** (Figure S8). The ESI-MS(−) spectrum of pure **Cu_3-Cu_{27}** in CH_3CN confirms that there are no larger nanojar sizes present (Figure S6). We conclude that solvents with smaller donor numbers (DN),[88] such as THF (DN = 20) used for the synthesis and CH_3CN (DN = 14) used for mass spectrometry, do not scramble pure **Cu_3-Cu_{27}** into other nanojar sizes at a considerable rate at ambient temperature, whereas the scrambling is much faster in DMSO (DN = 30) under similar conditions. After sitting in CH_3CN for longer periods of time

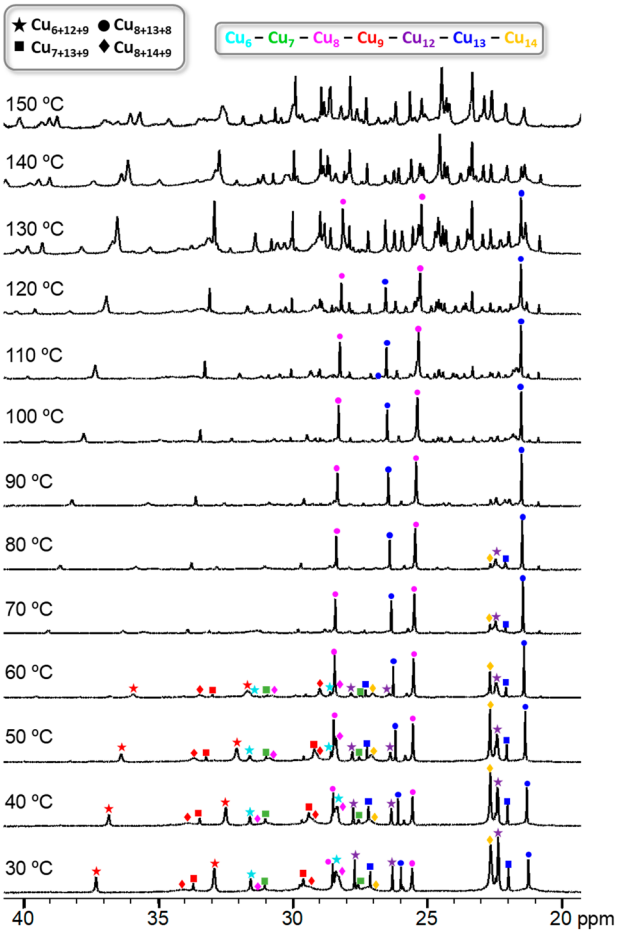

Figure 4. Variable-temperature ^{1}H NMR spectra of **Cu_3-Cu_n** in DMSO-d_6.

(months), **Cu_{27}** does slowly scramble and increasing amounts of **Cu_{29}** are observed besides **Cu_{27}** in the ESI-MS(−) spectrum of the aging solution. Nanojar size scrambling in the opposite direction has also been documented. Some batches of as-synthesized **Cu_3-Cu_n** consist of a mixture with n = 29, 30, and 31 and negligible amounts of n = 27 (Figure S9a). Upon dissolution of this mixture in DMSO, however, scrambling is observed: the distribution of nanojar sizes changes and the new mixture contains sizable amounts of n = 27 (Figure S9b). Moreover, if the ESI-MS(−) spectrum of an as-synthesized **Cu_3-Cu_n** mixture lacking n = 27 is recorded in DMF (DN = 27) as the solvent, **Cu_3-Cu_{27}** is present along with other capped nanojars of different sizes.

Besides the nanojar peaks described above, another pair of signals at 37.2 and 22.2 ppm appears upon the addition of NH_3 to the DMSO-d_6 solution of **Cu_3-Cu_{27}** (Figure 5). These signals correspond to the trinuclear species $[Cu_3O(pz)_3L_3]^+$ (L = NH_3 or solvent molecule), supported by the observation that a bulk sample of **Cu_3-Cu_n** dissolved in DMSO and saturated with NH_3 was found after 11 days to show only these two signals and no nanojar signals in the ^{1}H NMR spectrum (Figure S10). Mass spectrometry of this sample confirms the absence of nanojars by ESI-MS(−) and the presence of a trinuclear species by ESI-MS(+) at m/z 408, corresponding to $[Cu_3O(pz)_3]^+$ (Figure S11).

In the case of the NH_3 treatment of **Cu_n**, minor signals of the $[Cu_3O(pz)_3L_3]^+$ cap can also be observed at 37.3 and 22.3

https://doi.org/10.1021/acs.inorgchem.1c01826
Inorg. Chem. 2021, 60, 13479−13492

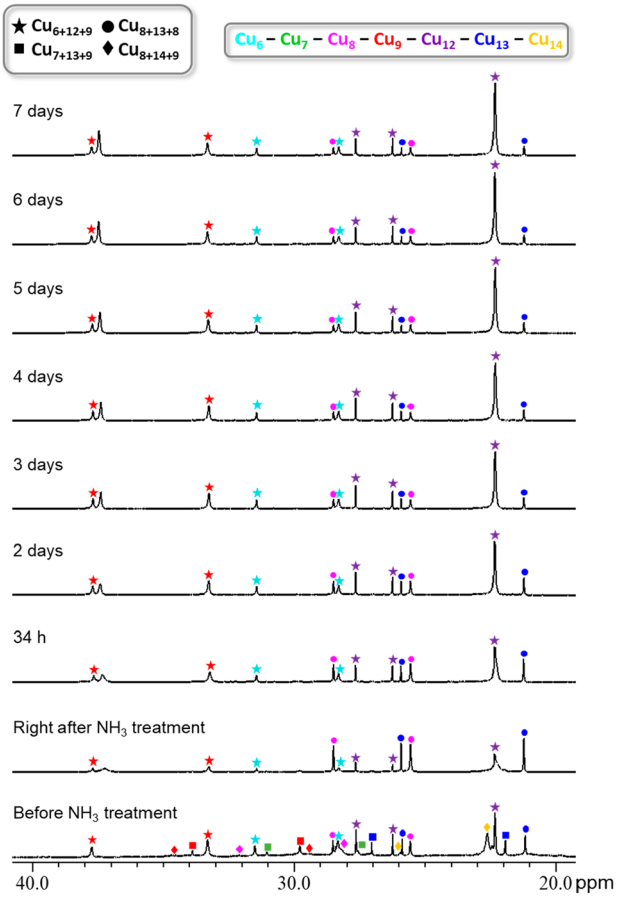

Figure 5. ^{1}H NMR monitoring of the NH_3-etching process of **Cu_3-Cu_n** in DMSO-d_6 over time.

ppm in the ^{1}H NMR spectrum (Figure S7). As described above (eq 3), small amounts of the capped nanojar **Cu_3-Cu_{27}** form during the conversion of **Cu_n** to **Cu_{27}**.

UV–Vis Spectroscopy. Figure 6 indicates that **Cu_3-Cu_n** and **Cu_n** have very similar absorption profiles. At the same concentration, the intensities of the peaks corresponding to d–d transitions (λ_{max} = 600 nm) are almost identical for **Cu_3-Cu_n**

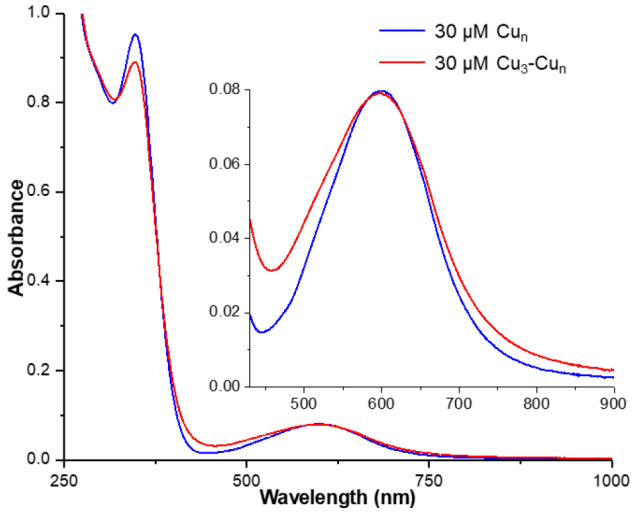

Figure 6. UV–vis spectra in CH_3CN of **Cu_3-Cu_n** (red trace) and **Cu_n** (blue trace).

and **Cu_n**, while the intensity of the peak attributed to charge transfer (λ_{max} = 350 nm) is slightly higher for **Cu_n**, indicating a slightly larger component of charge transfer in the case of **Cu_n**.

Elemental Analysis. To obtain further proof for the composition of capped nanojars and to demonstrate the absence of organic counterions, elemental analysis was carried out for **Cu_3-Cu_n** and compared to that of **Cu_{27}**. A sample of **Cu_3-Cu_n** (n = 27, 29, 30, and 31) was purified by recrystallization from THF by the addition of hexane and dried in high vacuum. The obtained elemental analysis values of 25.94% C, 2.52% H, and 18.09% N are in good agreement with the formula $[\{Cu_3(OH)(pz)_3(THF)_3\}CO_3\{Cu(OH)(pz)\}_{29}]$ (calcd for $C_{109}H_{150}Cu_{32}N_{64}O_{36}$: C, 26.36; H, 3.04; N, 18.05). An average size of n = 29 is considered for **Cu_3-Cu_n**; other values of n (27–31) give similar calculated C/H/N values (identical within experimental error). In contrast, elemental analysis of **Cu_{27}** (obtained from **Cu_n** by etching with NH_3[76] and purified by repeated recrystallization from toluene by hexane vapor diffusion, followed by drying in high vacuum) yields very different values of 31.72% C, 3.83% H, and 16.69% N, which agree well with the formula $(Bu_4N)_2[CO_3\{Cu(OH)(pz)\}_{27}](toluene)$ (calcd for $C_{121}H_{188}Cu_{27}N_{56}O_{30}$: C, 31.44; H, 4.10; N, 16.97).

Crystallographic Description. Two different crystals of the capped nanojar **Cu_3-Cu_{27}** have been obtained: $[\{Cu_3(\mu_3\text{-}OH)(\mu\text{-}pz)_3(DMF)_3\}CO_3\subset\{Cu(\mu\text{-}OH)(\mu\text{-}pz)\}_{27}]$ (**1**; monoclinic $C2/c$, one independent capped nanojar per asymmetric unit) by slow evaporation of a DMF solution of **Cu_3-Cu_n** and $[\{Cu_3(\mu_3\text{-}OH)(\mu\text{-}pz)_3(CH_3CN)_3\}CO_3\subset\{Cu(\mu\text{-}OH)(\mu\text{-}pz)\}_{27}]$ (**2**; monoclinic $P2_1/n$, two independent capped nanojars per asymmetric unit) from a CH_3CN solution of **Cu_n** upon standing with 2 equiv of HNO_3 added. Because the structures of **1** and **2** are almost identical (Figure S12), structural details will only be discussed for **1** in the following paragraphs; the corresponding values for **2** are shown in Table S1.

The capped nanojar is located on a general position and displays pseudo-3-fold symmetry (Figures 7 and 8). Its structure is closely related to that of **Cu_{27}**, in which three neutral $[cis\text{-}Cu^{II}(\mu\text{-}OH)(\mu\text{-}pz)]_n$ rings (n = 6 + 12 + 9) define the nanojar, with its cavity occupied by an incarcerated carbonate ion.[76] As shown in Figure 9, the same Cu_6 + Cu_{12} + Cu_9 ring combination is found in both **Cu_{27}** and **Cu_3-Cu_{27}**, which are almost superimposable. The central, larger Cu_{12} ring is approximately flat; its pyrazolate units symmetrically alternate above and below the ring mean plane (reflected in two different sets of pyrazolate ^{1}H NMR signals), and it does not form hydrogen bonds with the carbonate ion. The smaller Cu_6 and Cu_9 side rings are bowl-shaped, with their pyrazolate moieties pointing away from the central ring, while their OH groups point toward the center of the nanojar and form multiple hydrogen bonds with the incarcerated carbonate ion. Although there is no direct bonding between the two smaller rings, they are both involved in multiple hydrogen bonds and axial Cu···O interactions with the larger central ring. In the $[cis\text{-}Cu^{II}(\mu\text{-}OH)(\mu\text{-}pz)]_n$ rings, the Cu–O and Cu–N bond lengths are within normal ranges, 1.905(6)–1.956(6) and 1.944(8)–2.028(8) Å, respectively (Tables S2–S4). While in **Cu_{27}** the 2– charge of the incarcerated carbonate ion is balanced by two Bu_4N^+ counterions, in **Cu_3-Cu_{27}**, it is the additional bonded $[Cu_3(OH)(pz)_3(DMF)_3]^{2+}$ moiety that renders the assembly neutral. This trinuclear moiety binds to O atoms of the Cu_9 ring by three weak, axial Cu–O bonds

https://doi.org/10.1021/acs.inorgchem.1c01826
Inorg. Chem. 2021, 60, 13479–13492

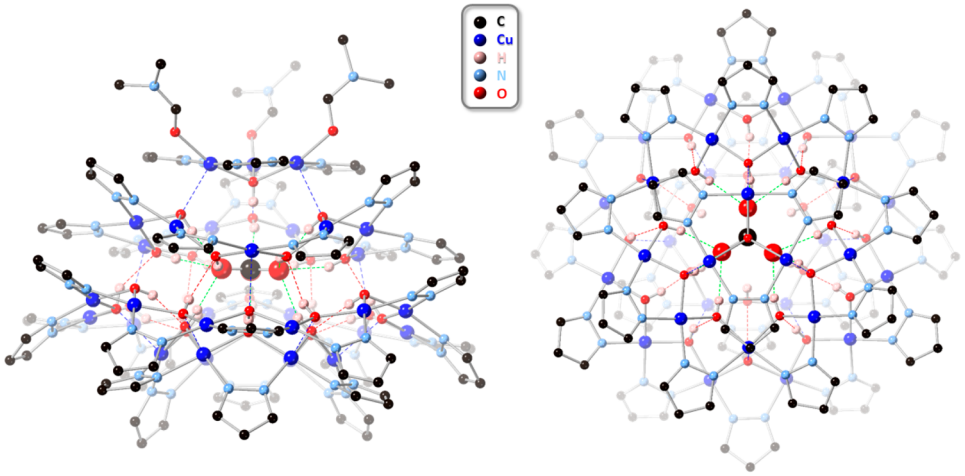

Figure 7. Ball-and-stick representation of the crystal structure of $\mathbf{Cu_3}$-$\mathbf{Cu_{27}}$ (left, side view; right, top view). Color code for hydrogen bonding: O−H···O between Cu_m rings, red; O−H···O between Cu_m rings and carbonate, green. Axial Cu···O interactions are shown in blue. Lattice solvent molecules and C−H bond H atoms are omitted for clarity, and only one component is shown for disordered pyrazolate and DMF moieties.

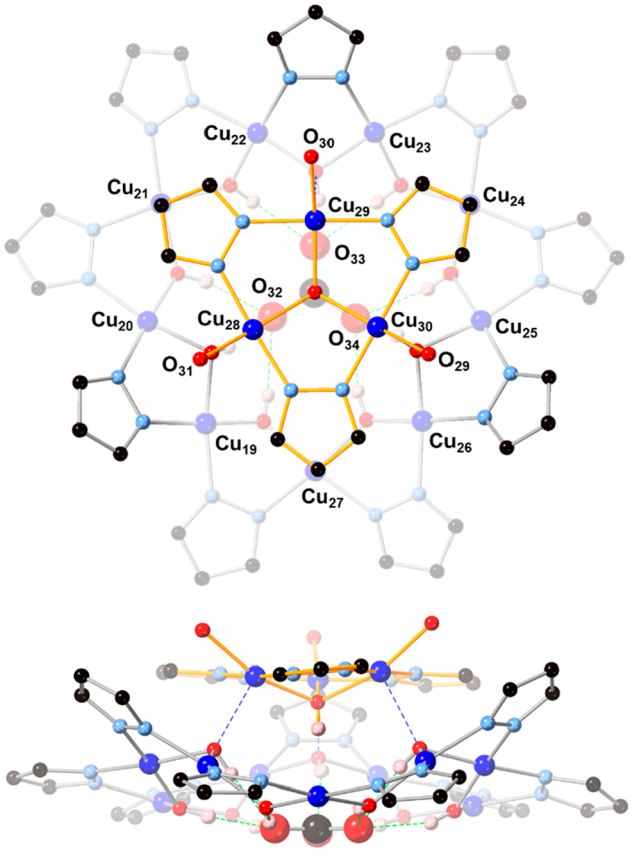

Figure 8. Top and side views of the binding of the $[Cu_3(\mu_3\text{-}OH)(\mu\text{-}pz)_3(DMF)_3]^{2+}$ "cap" to the $[Cu(\mu\text{-}OH)(\mu\text{-}pz)]_9$ ring in $\mathbf{Cu_3}$-$\mathbf{Cu_{27}}$. The trinuclear moiety is highlighted in orange (C−H bond H atoms are omitted, and only the O atoms of coordinated DMF molecules are shown).

[2.338(6), 2.399(6), and 2.470(6) Å; Figure 8]. A related "cap" was observed in $Bu_4N[\{Cu_3(\mu_3\text{-}OCH_3)(\mu\text{-}pz)_3\}\text{-}PO_4\subset\{Cu(\mu\text{-}OH)(\mu\text{-}pz)\}_{27}(CH_3OH)_2]$.[78] In this structure, however, the trinuclear unit is strongly bound to the nanojar [Cu−O bonds lengths: 1.982(9), 1.980(8), and 1.992(9) Å], the μ_3-OCH_3 moiety points outward (whereas in $\mathbf{Cu_3}$-$\mathbf{Cu_{27}}$, the μ_3-OH moiety points inward), and the PO_4^{3-} ion directly binds to the Cu atoms of the trinuclear unit [Cu−O bond lengths: 2.303(9), 2.327(9), and 2.480(9) Å]. It is also apparent that here the 2+ charged trinuclear unit binds to the nanojar in order to reduce the large 3− charge of the phosphate ion and not because of a weak base used for the synthesis (NaOH was employed) or a lack of Bu_4N^+ counterions.

As in $\mathbf{Cu_{27}}$, the OH groups of the Cu_{12} ring in $\mathbf{Cu_3}$-$\mathbf{Cu_{27}}$ donate 12 alternating hydrogen bonds, six to the Cu_6 ring [O···O = 2.703(12)−2.762 (9) Å; average = 2.732(9) Å] and six to the Cu_9 ring [O···O = 2.752(8)−2.785(9) Å; average = 2.769(9) Å], with an overall average of 2.751(9) Å (Tables S5−S7). The corresponding overall average of the 12 O···O distances in $\mathbf{Cu_{27}}$ is virtually identical [2.761(5) Å]. Similarly, the incarcerated carbonate ion forms 12 hydrogen bonds (four for each O atom) with OH groups of the Cu_6 and Cu_9 rings, which average 2.818(9) Å [range 2.773(8)−2.873(9) Å] in $\mathbf{Cu_3}$-$\mathbf{Cu_{27}}$ and 2.842(5) Å [range 2.746(5)−2.915(5) Å] in $\mathbf{Cu_{27}}$.

The Cu_6 and Cu_9 rings in $\mathbf{Cu_3}$-$\mathbf{Cu_{27}}$ form six and three Cu··· O contacts with O atoms of the Cu_{12} ring, respectively [Cu_6 ring, Cu···O = 2.392(6)−2.451(8) Å, average = 2.421(8) Å; Cu_9 ring, Cu···O = 2.407(6)−2.412(6) Å; average = 2.410(6) Å]. All other Cu atoms are at distances larger than the sum of the van der Waals radii of Cu and O (2.92 Å) from the closest nonbonding O atoms [Cu···O = 3.008(5)−3.230(6) Å]. Overall, there are nine Cu···O distances <2.92 Å between Cu_n rings, with an average of 2.415(6) Å. The corresponding value for $\mathbf{Cu_{27}}$ is 2.388(4) Å [Cu_6 ring, Cu···O = 2.392(4)−2.487(4) Å, average = 2.415(4) Å; Cu_9 ring, Cu···O = 2.352(4)−2.368(4) Å; average = 2.362(4) Å].

pH-Controlled, Stepwise Assembly−Disassembly of Nanojars. In an earlier study, we had shown that $Cu(NO_3)_2$ and pyrazole are in a pH-dependent equilibrium with nanojars.[86] Even in the absence of an additional base, a trinuclear complex, $[Cu_3(\mu_3\text{-}OH)(\mu\text{-}pz)_3(NO_3)_3]^-$, partially forms in a solution of $Cu(NO_3)_2$ and pyrazole (3:3 molar ratio). Upon the addition of 4 equiv of NaOH to this mixture, the pure trinuclear intermediate $[Cu_3(\mu_3\text{-}OH)(\mu\text{-}pz)_3(NO_3)_2(H_2O)]$ can be isolated. The addition of 2 equiv more of NaOH cleanly converts the trinuclear intermediate to

https://doi.org/10.1021/acs.inorgchem.1c01826
Inorg. Chem. 2021, 60, 13479−13492

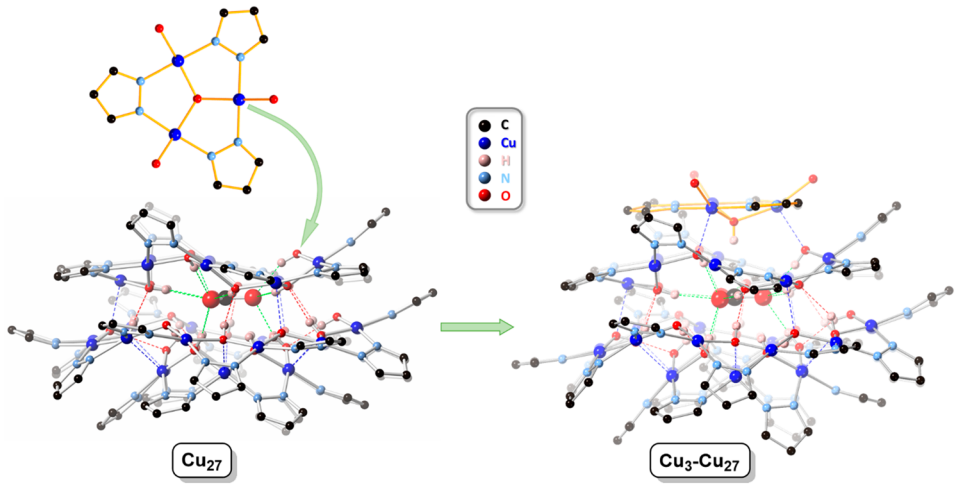

Figure 9. Comparison of the crystal structures of $\mathbf{Cu_{27}}$ and $\mathbf{Cu_3}$-$\mathbf{Cu_{27}}$, illustrating the conceptual formation of the latter from the former by the incorporation of a $[Cu_3(\mu_3\text{-}OH)(\mu\text{-}pz)_3(DMF)_3]^{2+}$ moiety (the curved arrow is intended to show the position of binding, not the mechanism). The trinuclear moiety is highlighted in orange (only the O atom of the DMF molecules is shown; C−H bond H atoms are omitted).

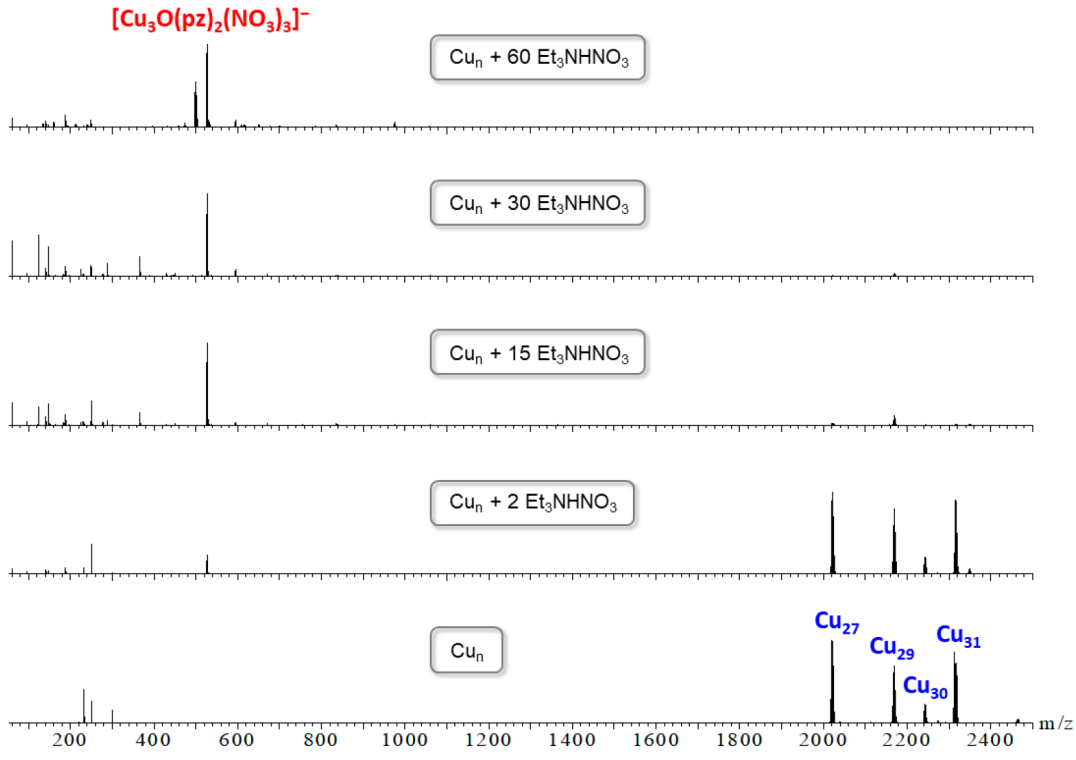

Figure 10. ESI-MS(−) monitoring of the titration of nanojars ($\mathbf{Cu_n}$) with increasing amounts of Et_3NHNO_3.

nanojars ($\mathbf{Cu_n}$). Analogously, the addition of gradually increasing amounts of HNO_3 to a solution of $\mathbf{Cu_n}$ led to conversion back to the trinuclear complex and eventually to Cu^{2+} ions and pyrazole in the presence of excess HNO_3.

In this work, we have identified and isolated another intermediate in the pH-dependent assembly−disassembly of nanojars, namely, capped nanojars $\mathbf{Cu_3}$-$\mathbf{Cu_n}$ (n = 27, 29, 30, and 31). As shown in Figure 10, titration with $Et_3NH^+NO_3^-$ converts $\mathbf{Cu_n}$ first to $\mathbf{Cu_3}$-$\mathbf{Cu_n}$ and then to $[Cu_3(\mu_3\text{-}OH)(\mu\text{-}pz)_3(NO_3)_3]^-$. The addition of 2 equiv of Et_3NH^+ leads to the appearance of a new peak in the ESI-MS(−) spectrum at m/z 527 corresponding to $[Cu_3O(pz)_2(NO_3)_3]^-$, along with peaks corresponding to $\mathbf{Cu_n}$ (n = 27, m/z 2023; n = 29, m/z 2171; n = 30, m/z 2245; n = 31, m/z 2318). As described above, these peaks originate from both $\mathbf{Cu_n}$ and $\mathbf{Cu_3}$-$\mathbf{Cu_n}$ upon ionization by detachment of the $\mathbf{Cu_3}^{2+}$ cap. In the presence of larger amounts of Et_3NH^+, the nanojar peaks gradually disappear, while the peak corresponding to the trinuclear intermediate intensifies. The addition of 60 equiv of Et_3NH^+ (which would be present in solution if nanojars formed from the reaction of copper nitrate, pyrazole, and Et_3N in a 1:1:2 molar ratio before the THF solution was poured into excess water) shows complete conversion of nanojars to the trinuclear species (eq 5), as is evidenced by the complete absence of nanojar peaks in

https://doi.org/10.1021/acs.inorgchem.1c01826
Inorg. Chem. 2021, 60, 13479−13492

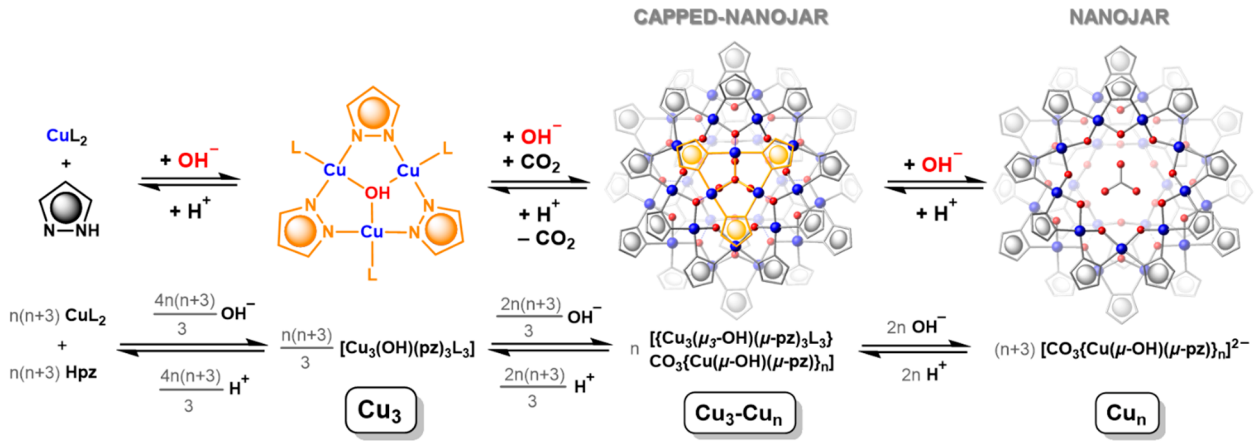

Figure 11. Illustration of the pH-dependent equilibrium between Cu^{2+} and pyrazole, trinuclear copper pyrazolate complex **Cu_3**, capped nanojars **Cu_3-Cu_n**, and nanojars **Cu_n** (n = 27 is shown). In the trinuclear complex, L is the counterion of CuL_2, whereas in the capped nanojar, L is a neutral donor molecule.

the ESI-MS(−) spectrum and the presence of a major peak corresponding to the trinuclear complex. This result further demonstrates that nanojars cannot form in solution in the presence of acidic Et_3NH^+ ions.

$$(Bu_4N)_2[CO_3\{Cu(\mu\text{-}OH)(\mu\text{-}pz)\}_n] + (n+2)(Et_3NH)NO_3 \rightarrow \frac{n}{3}Et_3NH[Cu_3(\mu_3\text{-}OH)(\mu\text{-}pz)_3(NO_3)_3] + \frac{2(n+3)}{3}Et_3N + CO_2 + H_2O + 2(Bu_4N)NO_3 \quad (5)$$

Previously, we had demonstrated the stepwise conversion of $Cu(NO_3)_2$ and pyrazole to nanojars via a trinuclear intermediate, and vice versa.[86] Herein we further demonstrate that capped nanojars can be reversibly converted to nanojars. Given their vastly different solubilities, the conversion of capped nanojars to nanojars was investigated by the addition of Bu_4NOH, which is expected to transform sparingly soluble **Cu_3-Cu_n** into highly soluble **Cu_n** according to eq 6. Indeed, the addition of 2 equiv of Bu_4NOH to a suspension of **Cu_3-Cu_n** in CH_3CN led to the immediate and complete dissolution of the solid. ESI-MS(−) of the clear solution shows the presence of **Cu_n** (n = 27, 29, 30, and 31; Figure S13). Similarly, the addition of 1 equiv of $(Bu_4N)_2SO_4$ to a suspension of **Cu_3-Cu_n** in CH_3CN also led to immediate dissolution. The ESI-MS(−) spectrum of the resulting clear solution shows new peaks corresponding to sulfate nanojars (**Cu_{28}**, m/z 2115; **Cu_{31}**, m/z 2336; **Cu_{33}**, m/z 2484), in addition to carbonate nanojar peaks at m/z 2023 (**Cu_{27}**), m/z 2171 (**Cu_{29}**), and m/z 2245 (**Cu_{30}**) (Figure S13). Noteworthy here is the complete disappearance of the peak at m/z 2318, corresponding to the carbonate nanojar **Cu_{31}**. It had been shown earlier that the **Cu_{31}** nanojar easily exchanges carbonate for sulfate because the larger size of sulfate is more complementary to the cavity size of the **Cu_{31}** nanojar.[77]

$$n[\{Cu_3(\mu_3\text{-}OH)(\mu\text{-}pz)_3L_3\}CO_3\{Cu(\mu\text{-}OH)(\mu\text{-}pz)\}_n] + 2(n+3)Bu_4NOH + 3CO_2 \rightarrow (n+3)(Bu_4N)_2[CO_3\{Cu(\mu\text{-}OH)(\mu\text{-}pz)\}_n] + 3nL + 3H_2O \quad (6)$$

The conversion of nanojars to capped nanojars was demonstrated by treating an CH_3CN solution of nanojars with 2 equiv of HNO_3. Upon standing in a closed vessel (no solvent evaporation), dark-blue single crystals formed and the blue color of the solution became substantially lighter. X-ray diffraction shows that the obtained compound (**2**) has a structure identical with that of **1** described above, except with CH_3CN instead of DMF solvent molecules (Figure S12). The nanojar-to-capped-nanojar transformation is quantified by eq 7. Figure 11 summarizes the stepwise assembly−disassembly of nanojars, including balanced equations for each step.

$$(n+3)(Bu_4N)_2[CO_3\{Cu(\mu\text{-}OH)(\mu\text{-}pz)\}_n] + 2(n+3)HNO_3 \xrightarrow{CH_3CN} n[\{Cu_3(\mu_3\text{-}OH)(\mu\text{-}pz)_3(CH_3CN)_3\}\text{-}CO_3\{Cu(\mu\text{-}OH)(\mu\text{-}pz)\}_n] + 3CO_2 + 2nH_2O + 2(n+3)(Bu_4N)NO_3 \quad (7)$$

Alternative Solvents and Bases for Capped-Nanojar Synthesis. For practical purposes and eventual large-scale applications, the use of less volatile solvents and bases that are less prone to considerable loss by evaporation would be advantageous. Thus, the synthesis of capped nanojars was also performed in DMF at 20 °C (vapor pressure 0.36 kPa and boiling point 153 °C) instead of THF (vapor pressure 19.1 kPa and boiling point 65 °C), with virtually identical results. Propylene carbonate (vapor pressure 0.018 kPa, boiling point 240 °C, and flash point 132 °C), which is considered to be a green solvent[89] (odorless, nontoxic, biodegradable, and obtained from propylene oxide and CO_2), was also employed successfully for the synthesis of capped nanojars.

Similar results were also obtained when using $^nBu_3N$ (vapor pressure 0.04 kPa and boiling point 216 °C) or $^nOct_3N$ (vapor pressure <0.001 kPa and boiling point 365 °C) instead of Et_3N

https://doi.org/10.1021/acs.inorgchem.1c01826
Inorg. Chem. 2021, 60, 13479−13492

(vapor pressure 6.90 kPa and boiling point 89 °C). The former two bases present additional advantages because they are less soluble in water ($^{n}Bu_3N$, 50 mg/L; $^{n}Oct_3N$, 0.050 mg/L) and are less flammable (flash point: $^{n}Bu_3N$, 63 °C; $^{n}Oct_3N$, 168 °C) than Et_3N (solubility 112.4 g/L and flash point −11 °C).

Regarding the base used for capped-nanojar synthesis, the following question arose during these studies: can capped nanojars be obtained in an organic solvent using soluble, organic bases without having to transfer the conjugate acid byproduct to water by either precipitation of the capped nanojar or liquid−liquid extraction? Because trialkylamines are weak bases, the corresponding trialkylammonium conjugate acids are relatively strong. Et_3NH^+ has a pK_a value of 12.5 in THF (the reaction solvent employed) and 18.83 in CH_3CN (the solvent used for mass spectrometric analysis).[90] Therefore, a much stronger organic base is needed for the conjugate acid to be weak enough to be tolerated by the capped nanojar. *N*,*N*,*N*′,*N*′-Tetramethylguanidine (TMG; pK_{aH} 15.5 in THF and 23.35 in CH_3CN) and 1,8-diazabicyclo[5.4.0]undec-7-ene (DBU; pK_{aH} 16.9 in THF and 24.31 in CH_3CN), for example, are approximately 3−4 and 5−6 orders of magnitude stronger than Et_3N in THF and CH_3CN, respectively.[90] The ESI-MS(−) spectrum of the solution obtained from $Cu(NO_3)_2\cdot 2.5H_2O$, pyrazole, and DBU (1:1:2 molar ratio) in THF shows a major peak at *m*/*z* 527 corresponding to the trinuclear species $[Cu_3O(pz)_2(NO_3)_3]^-$, whereas nanojar peaks are barely detectable (Figure S14). The corresponding reaction mixture obtained with TMG also has *m*/*z* 527 as the base peak, but nanojars are now clearly observable (Figure S15). When the even stronger base 1,5,7-triazabicyclo[4.4.0]dec-5-ene (TBD; pK_{aH} 21.0 in THF and 26.02 in CH_3CN; 8 and 7 orders of magnitude stronger than Et_3N in THF and CH_3CN, respectively)[90] is used, the ESI-MS(−) spectrum shows that nanojars are now more abundant than the trinuclear complex (Figure S16). All three reaction mixtures in THF described above provided the capped-nanojar mixture **Cu$_3$-Cu$_n$** upon precipitation with excess water. However, to completely convert the trinuclear species into capped nanojars in an organic solvent alone, an even stronger organic base, such as a phosphazene base (e.g., $EtP_2(dma)_5$, pK_{aH} 25.3 in THF and 32.94 in CH_3CN; $^{t}BuP_4(dma)_9$, pK_{aH} 33.9 in THF and 42.7 in CH_3CN)[90] would be needed.

Atmospheric CO_2 Sequestration and Selective Carbonate Binding. During the self-assembly of capped nanojars from a copper(II) salt (nitrate, perchlorate, tetrafluoroborate, chloride, or bromide), pyrazole, and Et_3N (or another organic base), CO_2 is selectively sequestered from the air in the presence of other atmospheric gases and is converted to carbonate. The binding of the CO_3^{2-} ion is selective in the presence of NO_3^-, ClO_4^-, BF_4^-, Cl^-, and Br^- because none of these anions were found in the product. Because the empty nanojar/capped-nanojar host does not exist without an incarcerated anion guest, the measurement of an association constant by host−guest titration experiments is impossible. Instead, we assessed the carbonate binding strength of nanojars and capped nanojars by conducting a competition experiment with Ba^{2+}. The precipitation of insoluble $BaCO_3$ ($K_{sp} = 2.58 \times 10^{-9}$ at 25 °C in water) would be expected if the CO_3^{2-} ion dissociated from the nanojar, accompanied by the collapse of the nanojar host, leading to the precipitation of insoluble, polymeric $[Cu(OH)(pz)]_\infty$. First, solutions of **Cu$_3$** and **Cu$_3$-Cu$_n$** in butyronitrile were stirred with aqueous solutions of $Ba(NO_3)_2$. No precipitation or any other visible changes were observed after 16 h. Further experiments were conducted under homogeneous conditions in THF using barium dioctyl sulfosuccinate, $Ba(DOSS)_2$, which is soluble in THF together with the nanojar/capped-nanojar mixture. Similarly to the heterogeneous butyronitrile/water system, no changes were observed upon standing for 16 h, and ESI-MS(−) spectra indicate that the nanojar/capped-nanojar mixture is unaffected (Figures S17 and S18).

CO_2 can be regenerated from the carbonate-incarcerating capped nanojars by treatment with a weak acid, according to eq 8, which also shows that the process is reversible. After acidification and liberation of CO_2, the solution containing the trinuclear copper pyrazolate species can be recycled: capped nanojars re-form as the pH is raised upon the addition of a base.

$$n[\{Cu_3(\mu_3\text{-}OH)(\mu\text{-}pz)_3L_3\}CO_3\{Cu(\mu\text{-}OH)(\mu\text{-}pz)\}_n] \underset{2n(n+3)/3OH^-}{\overset{2n(n+3)/3H^+}{\rightleftharpoons}} \frac{n(n+3)}{3}[Cu_3(\mu_3\text{-}OH)(\mu\text{-}pz)_3L_3]^- + nCO_2 \quad (8)$$

CONCLUSIONS

In this work, we demonstrate that if weak bases such as NH_3 or trialkylamines are used instead of NaOH or Bu_4NOH for the synthesis from a copper(II) salt and pyrazole, capped nanojars $[\{Cu_3(OH)(pz)_3L_3\}CO_3C\{Cu(OH)(pz)\}_n]$ (**Cu$_3$-Cu$_n$**; *n* = 27, 29, 30, and 31; L = neutral donor ligand) are obtained instead of the conventional nanojars $[CO_3C\{Cu(OH)(pz)\}_n]^{2-}$ (**Cu$_n$**). An array of characterization techniques including ESI-MS, UV−vis and variable-temperature ^1H NMR spectroscopy, elemental analysis, and single-crystal X-ray diffraction were employed along with reactivity and solubility studies to characterize **Cu$_3$-Cu$_n$** species in solution and the solid state. These studies show that capped nanojars are an extension of the $[CO_3C\{Cu(\mu\text{-}OH)(\mu\text{-}pz)\}_n]^{2-}$ motif, with a $[Cu_3(OH)(pz)_3L_3]^{2+}$ moiety that is either bound in the solid state and slightly polar solvents or detached in highly polar solvents. Although capped nanojars cannot be observed directly by ESI-MS because of their overall charge-neutrality, ionization by loss of the $[Cu_3(OH)(pz)_3L_3]^{2+}$ cap does lead to $[CO_3C\{Cu(\mu\text{-}OH)(\mu\text{-}pz)\}_n]^{2-}$ daughter species in ESI-MS(−). ESI-MS(+), on the other hand, confirms the presence of the detached cap in the form of $[Cu_3O(pz)_3]^+$. The most dramatic difference upon going from **Cu$_n$** to **Cu$_3$-Cu$_n$**, with implications in the use of nanojars as anion binding and extracting agents, as well as CO_2-sequestering agents, is the drastic reduction of solubility in organic solvents: in THF, for example, the solubility is reduced over 150-fold. The discovery of capped nanojars sheds light on elusive previous observations, such as those involved in the NH_3 etching of nanojars, and uncovers an important new intermediate in the pH-controlled assembly−disassembly of nanojars. CO_2 is selectively sequestered from the air in the presence of other atmospheric gases and is converted to carbonate during the self-assembly of capped nanojars. We have shown that the CO_3^{2-} ion is bound very strongly by a multitude of charge-assisted hydrogen bonds that wrap around the anion and totally isolate it from its surrounding medium. The binding of carbonate by capped nanojars is selective in the presence of NO_3^-, ClO_4^-, BF_4^-, Cl^-, and Br^- ions. Future studies will

https://doi.org/10.1021/acs.inorgchem.1c01826
Inorg. Chem. 2021, 60, 13479−13492

address conversion of the captured CO_2 to value-added products.

EXPERIMENTAL SECTION

General Procedures. All commercially available chemicals were used as received. Gaseous NH_3 was generated from a 28−30% aqueous ammonium hydroxide solution by gentle warming. UV−vis and NMR spectra were collected on a Shimadzu UV-1650PC spectrophotometer and a Jeol JNM-ECZS (400 MHz) instrument, respectively.

Synthesis of $[Cu_3(OH)(pz)_3(H_2O)_3][CO_3\subset\{Cu(OH)(pz)\}_n]$ (Cu_3-Cu_n; n = 27, 29, 30, and 31). $Cu(NO_3)_2\cdot 2.5H_2O$ (3.0000 g, 12.90 mmol) and pyrazole (0.8781 g, 12.90 mmol) were dissolved in THF (50 mL) in a 100 mL round-bottom flask. To the clear, blue solution was added dropwise, under stirring, Et_3N (99%; 4 mL, 2.9040 g, 28.41 mmol). The resulting clear, dark-blue solution was stirred for 30 min and then added in small portions to 500 mL of water under stirring. The resulting mixture was stirred overnight (∼14 h) in an uncovered beaker. The blue precipitate was filtered out, washed thoroughly with water, and dried under vacuum. Yield: 2.0425 g (97%). Similar results were obtained when $Cu(ClO_4)_2\cdot 6H_2O$, $Cu(BF_4)_2\cdot 6H_2O$, $CuCl_2\cdot 2H_2O$, or $CuBr_2$ were used instead of $Cu(NO_3)_2\cdot 2.5H_2O$. A small extent of partial bromination of the pyrazole ring was observed in the case of $CuBr_2$.

Reaction of Cu_3-Cu_n with Bu_4NOH and $(Bu_4N)_2SO_4$. In three 10 mL round-bottom flasks, suspensions of slightly soluble **Cu_3-Cu_n** (0.0500 g, 0.0105 mmol) in CH_3CN (5 mL) were prepared under stirring. The first flask was kept as a control, whereas Bu_4NOH (55% in water, 10.0 μL, 9.95 mg, 0.0210 mmol) and $(Bu_4N)_2SO_4$ (50% in water, 12.2 μL, 12.20 mg, 0.0105 mmol) were added to the second and third flasks, respectively. An immediate dissolution of the suspension was observed in the second and third flasks, accompanied by a significant intensification of the blue color of the solution, whereas the contents of the control flask remained unchanged after stirring for 24 h. ESI-MS(−) spectra of the resulting solutions are shown in Figure S13.

Etching of Cu_3-Cu_n with NH_3. **Cu_3-Cu_n** (0.0200 g, 4.20×10^{-3} mmol) was dissolved in THF (50 mL) in a 100 mL round-bottom flask. NH_3 gas was bubbled through the solution under stirring for 15 min. After standing for 12 days in a sealed flask, an aliquot was taken for ESI-MS analysis. The ESI-MS(−) spectrum showed complete conversion of **Cu_3-Cu_n** to **Cu_3-Cu_{27}** (Figure S6). The reaction mixture was filtered and left to evaporate in air, leaving behind a solid, which was further dried under high vacuum to give 0.0172 g of a dark-blue powder.

Competitive Anion Binding under Heterogeneous Conditions. $Ba(NO_3)_2$ (1.0000 g, 3.82 mmol) was dissolved in water (12 mL) in a 50 mL round-bottom flask. **Cu_n** (0.0101 g, 2.10×10^{-3} mmol) or **Cu_3-Cu_n** (0.0100 g, 2.10×10^{-3} mmol) was dissolved in butyronitrile (25 mL). The $Ba(NO_3)_2$ solution was vigorously stirred with 12.5 mL of the **Cu_n**/**Cu_3-Cu_n** solution for 16 h. The remainder of the **Cu_n**/**Cu_3-Cu_n** solution (12.5 mL) was used as a control. The organic layer and control solution were analyzed by ESI-MS.

Competitive Anion Binding under Homogeneous Conditions. To a solution of **Cu_n** (0.0101 g, 2.10×10^{-3} mmol) or **Cu_3-Cu_n** (0.0100 g, 2.10×10^{-3} mmol) in THF (24.5 mL) was added $Ba(DOSS)_2$ (4.20 mM in THF, 500 μL, 2.10×10^{-3} mmol). A control solution was prepared by dissolving **Cu_n** (0.0101 g, 2.10×10^{-3} mmol) or **Cu_3-Cu_n** (0.0100 g, 2.10×10^{-3} mmol) in THF (25.0 mL). Aliquots were taken directly from the solutions and analyzed by ESI-MS.

Mass Spectrometry. Mass spectrometric analysis of the nanojars was performed with a Waters Synapt G1 HDMS instrument, using electrospray ionization. 10^{-4}−10^{-5} M solutions were prepared in CH_3CN or DMF. Samples were infused by a syringe pump at 5 μL/min, and nitrogen was supplied as the nebulizing gas at 500 L/h. The electrospray capillary voltage was set to −2.5 or +2.5 kV, respectively, with a desolvation temperature of 110 or 150 °C. The sampling and extraction cones were maintained at 40 and 4.0 V, respectively, at 80 °C. The in-source fragmentation analyses were conducted by only altering the sampling cone voltage and preserving all other conditions.

X-ray Crystallography. Single crystals of **Cu_3-Cu_{27}** were grown from a DMF solution by slow evaporation (**1**) and from a CH_3CN solution of **Cu_n** upon standing with 2 equiv of HNO_3 added (**2**). Once removed from the mother liquor, the crystals are very sensitive to solvent loss at ambient conditions and were mounted quickly under a cryostream (100 K for **1** and 150 K for **2**) to prevent decomposition. X-ray diffraction data were collected from a single crystal mounted atop a glass fiber under Paratone-N oil with a Bruker SMART APEX II diffractometer (for **1**) and from a single crystal mounted atop a MiTeGen micromesh mount under Fomblin oil with a Bruker AXS D8 Quest diffractometer equipped with a Photon II charge-integrating pixel array detector (for **2**) using graphite-monochromated Mo Kα (λ = 0.71073 Å) radiation. The data were integrated using *SAINT*[91] and scaled and corrected for absorption and other effects using *SADABS*.[92] The structures were solved by employing direct methods using *ShelXS*[93] and refined by full-matrix least squares on F^2 using *ShelXL*.[94] C−H bond H atoms were placed in idealized positions and refined using the riding model. Further refinement details, including the treatment of disorder, use of *SQUEEZE* (for **1**), and thermal ellipsoid plots (Figures S19 and S20), are provided in the Supporting Information.

Summary of the crystallographic data for **1**: chemical formula, sum, $C_{119.61}H_{188.10}Cu_{30}N_{69.54}O_{42.21}$; chemical formula, moiety, $(C_{99}H_{141}Cu_{30}N_{63}O_{32})(CO_3)(C_3H_7NO)_{6.536}(H_2O)_{0.678}$(solvent); formula weight, 5181.86; crystal system, monoclinic; space group, $C2/c$ (No. 15); a = 44.8101(10) Å; b = 33.2795(10) Å; c = 34.7234(11) Å; β = 125.983(3)°; V = 41901(2) Å^3; Z = 8; D_{calc} = 1.643 g/cm^3; μ = 3.048 mm^{-1}; no. of reflns collected, 665057; no. of unique reflns, 37531; no. of obsd reflns [$I > 2\sigma(I)$], 24605; R(int), 0.1236; data/parameters/restraints, 37531/2698/1453; goodness-of-fit (on F^2): 1.106; $R(F)$ [$I > 2\sigma(I)$], 0.0631; $R_w(F)$ [$I > 2\sigma(I)$], 0.1173; $R(F)$ (all data), 0.1511; $R_w(F)$ (all data), 0.1917; residual electron density, max/min (e/Å^3), 1.497/−0.868. Summary of the crystallographic data for **2**: chemical formula, sum, $C_{121.45}H_{163.68}Cu_{30}N_{75.22}O_{31}$; chemical formula, moiety, $(C_{96}H_{127}Cu_{30}N_{63}O_{28})(CO_3)(C_2H_3N)_{12.225}$; formula weight, 5079.69; crystal system, monoclinic; space group, $P2_1/n$ (No. 14); a = 31.6587(15) Å; b = 31.483(2) Å; c = 37.602(3) Å; β = 97.877(2)°; V = 37124(4) Å^3; Z = 8; D_{calc} = 1.818 g/cm^3; μ = 3.435 mm^{-1}; no. of reflns collected, 1179884; no. of unique reflns, 141707; no. of obsd reflns [$I > 2\sigma(I)$], 98223; R(int), 0.0763; data/parameters/restraints, 141707/5444/4355; goodness-of-fit (on F^2): 1.087; $R(F)$ [$I > 2\sigma(I)$], 0.0552; $R_w(F)$ [$I > 2\sigma(I)$], 0.0886; $R(F)$ (all data), 0.1395; $R_w(F)$ (all data), 0.1649; residual electron density, max/min (e/Å^3), 1.675/−1.224.

ASSOCIATED CONTENT

Supporting Information

The Supporting Information is available free of charge at https://pubs.acs.org/doi/10.1021/acs.inorgchem.1c01826.

Additional data for X-ray structure determination, mass spectrometry, and ^{1}H NMR spectroscopy (PDF)

Accession Codes

CCDC 2085518 and 2085519 contain the supplementary crystallographic data for this paper. These data can be obtained free of charge via www.ccdc.cam.ac.uk/data_request/cif, or by emailing data_request@ccdc.cam.ac.uk, or by contacting The Cambridge Crystallographic Data Centre, 12 Union Road, Cambridge CB2 1EZ, UK; fax: +44 1223 336033.

AUTHOR INFORMATION

Corresponding Author

Gellert Mezei − *Department of Chemistry, Western Michigan University, Kalamazoo, Michigan 49008, United States;*

https://doi.org/10.1021/acs.inorgchem.1c01826
Inorg. Chem. 2021, 60, 13479−13492

orcid.org/0000-0002-3120-3084; Email: gellert.mezei@wmich.edu

Authors

Wisam A. Al Isawi − *Department of Chemistry, Western Michigan University, Kalamazoo, Michigan 49008, United States*

Matthias Zeller − *Department of Chemistry, Purdue University, West Lafayette, Indiana 47907, United States;* orcid.org/0000-0002-3305-852X

Complete contact information is available at: https://pubs.acs.org/10.1021/acs.inorgchem.1c01826

Notes

The authors declare no competing financial interest.

■ ACKNOWLEDGMENTS

This material is based on work supported by the National Science Foundation under Grant CHE-1808554.

■ REFERENCES

(1) Tsui, E. Y.; Day, M. W.; Agapie, T. Trinucleating Copper: Synthesis and Magnetostructural Characterization of Complexes Supported by a Hexapyridyl 1,3,5-Triarylbenzene Ligand. *Angew. Chem., Int. Ed.* **2011**, *50*, 1668−1672.

(2) Lionetti, D.; Day, M. W.; Agapie, T. Metal-Templated Ligand Architectures for Trinuclear Chemistry: Tricopper Complexes and their O_2 Reactivity. *Chem. Sci.* **2013**, *4*, 785−790.

(3) Boča, R.; Dlháň, L.; Mezei, G.; Ortiz-Pérez, T.; Raptis, R. G.; Telser, J. Triangular, Ferromagnetically-Coupled Cu^{II}_3-Pyrazolato Complexes as Possible Models of Particulate Methane Monooxygenase (pMMO). *Inorg. Chem.* **2003**, *42*, 5801−5803.

(4) Rivera-Carrillo, M.; Chakraborty, I.; Mezei, G.; Webster, R. D.; Raptis, R. G. Tuning of the $[Cu_3(\mu\text{-O})]^{4+/5+}$ Redox Couple: Spectroscopic Evidence of Charge Delocalization in the Mixed-Valent $[Cu_3(\mu\text{-O})]^{5+}$ Species. *Inorg. Chem.* **2008**, *47*, 7644−7650.

(5) Spielberg, E. T.; Gilb, A.; Plaul, D.; Geibig, D.; Hornig, D.; Schuch, D.; Buchholz, A.; Ardavan, A.; Plass, W. A Spin-Frustrated Trinuclear Copper Complex Based on Triaminoguanidine with an Energetically Well-Separated Degenerate Ground State. *Inorg. Chem.* **2015**, *54*, 3432−3438.

(6) Fu, M.; Imai, T.; Han, T.-H.; Lee, Y. S. Evidence for a Gapped Spin-Liquid Ground State in a Kagome Heisenberg Antiferromagnet. *Science* **2015**, *350*, 655−658.

(7) Grundner, S.; Markovits, M. A. C.; Li, G.; Tromp, M.; Pidko, E. A.; Hensen, E. J. M.; Jentys, A.; Sanchez-Sanchez, M.; Lercher, J. A. Single-Site Trinuclear Copper Oxygen Clusters in Mordenite for Selective Conversion of Methane to Methanol. *Nat. Commun.* **2015**, *6*, 7546.

(8) Di Nicola, C.; Garau, F.; Karabach, Y. Y.; Martins, L. M. D. R. S.; Monari, M.; Pandolfo, L.; Pettinari, C.; Pombeiro, A. J. L. Trinuclear Triangular Copper(II) Clusters - Synthesis, Electrochemical Studies and Catalytic Peroxidative Oxidation of Cycloalkanes. *Eur. J. Inorg. Chem.* **2009**, *2009*, 666−676.

(9) Mimmi, M. C.; Gullotti, M.; Santagostini, L.; Battaini, G.; Monzani, E.; Pagliarin, R.; Zoppellaro, G.; Casella, L. Models for Biological Trinuclear Copper Clusters. Characterization and Enantioselective Catalytic Oxidation of Catechols by the Copper(II) Complexes of a Chiral Ligand Derived from (S)-(−)-1,1 '-Binaphthyl-2,2 '-diamine. *Dalton Trans.* **2004**, 2192−2201.

(10) Wang, L.; Guo, B.; Li, H.-X.; Li, Q.; Li, H.-Y.; Lang, J.-P. Polynuclear Copper(II) Pyrazolate Complexes: Temperature-Dependent Protonolysis Reactions, Crystal Structures and High Catalytic Activity Toward the Condensation of Nitriles with 2-Aminoalcohol. *Dalton Trans.* **2013**, *42*, 15570−15580.

(11) Bazzicalupi, C.; Bencini, A.; Bencini, A.; Bianchi, A.; Corana, F.; Fusi, V.; Giorgi, C.; Paoli, P.; Paoletti, P.; Valtancoli, B.; Zanchini, C. CO_2 Fixation by Novel Copper(II) and Zinc(II) Macrocyclic Complexes. A Solution and Solid State Study. *Inorg. Chem.* **1996**, *35*, 5540−5548.

(12) García-España, E.; Gaviña, P.; Latorre, J.; Soriano, C.; Verdejo, B. CO_2 Fixation by Copper(II) Complexes of a Terpyridinophane Aza Receptor. *J. Am. Chem. Soc.* **2004**, *126*, 5082−5083.

(13) Kong, L.-Y.; Zhang, Z.-H.; Zhu, H.-F.; Kawaguchi, H.; Okamura, T.; Doi, M.; Chu, Q.; Sun, W.-Y.; Ueyama, N. Copper(II) and Zinc(II) Complexes Can Fix Atmospheric Carbon Dioxide. *Angew. Chem., Int. Ed.* **2005**, *44*, 4352−4355.

(14) Liu, F.-L.; Kozlevčar, B.; Strauch, P.; Zhuang, G.-L.; Guo, L.-Y.; Wang, Z.; Sun, D. Robust Cluster Building Unit: Icosanuclear Heteropolyoxocopperate Templated by Carbonate. *Chem. - Eur. J.* **2015**, *21*, 18847−18854.

(15) Mateus, P.; Delgado, R.; Lloret, F.; Cano, J.; Brandão, P.; Félix, V. Trinuclear Copper(II) Cryptate and Its μ_3-CO_3 Cascade Complex: Thermodynamics, Structural and Magnetic Properties. *Chem. - Eur. J.* **2011**, *17*, 11193−11203.

(16) Das, B.; Bhadbhade, M.; Thapper, A.; Ling, C. D.; Colbran, S. B. A New Tri-Nuclear Cu-Carbonate Cluster Utilizing CO_2 as a C1-Building Block − Reactive Intermediates, a Probable Mechanism, and EPR and Magnetic Studies. *Dalton Trans.* **2019**, *48*, 3576−3582.

(17) Solomon, E. I.; Heppner, D. E.; Johnston, E. M.; Ginsbach, J. W.; Cirera, J.; Qayyum, M.; Kieber-Emmons, M. T.; Kjaergaard, C. H.; Hadt, R. G.; Tian, L. Copper Active Sites in Biology. *Chem. Rev.* **2014**, *114*, 3659−3853.

(18) Pandolfo, L.; Pettinari, C. Trinuclear Copper(II) Pyrazolate Compounds: A Long Story of Serendipitous Discoveries and Rational Design. *CrystEngComm* **2017**, *19*, 1701−1720.

(19) Guo, L.-Y.; Su, H.-F.; Kurmoo, M.; Wang, X.-P.; Zhao, Q.-Q.; Lin, S.-C.; Tung, C.-H.; Sun, D.; Zheng, L.-S. Multifunctional Triple-Decker Inverse 12-Metallacrown-4 Sandwiching Halides. *ACS Appl. Mater. Interfaces* **2017**, *9*, 19980−19987.

(20) Zueva, E. M.; Petrova, M. M.; Herchel, R.; Trávníček, Z.; Raptis, R. G.; Mathivathanan, L.; McGrady, J. E. Electronic Structure and Magnetic Properties of a Trigonal Prismatic Cu^{II}_6 Cluster. *Dalton Trans.* **2009**, 5924−5932.

(21) Mathivathanan, L.; Al-Ameed, K.; Lazarou, K.; Trávníček, Z.; Sanakis, Y.; Herchel, R.; McGrady, J. E.; Raptis, R. G. A Trigonal Prismatic Cu_6-Pyrazolato Complex Containing a μ_6-F Ligand. *Dalton Trans.* **2015**, *44*, 20685−20691.

(22) Shi, K.; Mathivathanan, L.; Raptis, R. G. Crystal Structure of μ_6-Chlorido-nonakis(μ-4-chloropyrazolato)bis-μ_3-methoxo-hexacopper(II). *Acta Crystallogr.* **2017**, *E73*, 266−269.

(23) Mezei, G.; Rivera-Carrillo, M.; Raptis, R. G. Trigonal-Prismatic Cu^{II}_6-Pyrazolato Cages: Structural and Electrochemical Study, Evidence of Charge Delocalization. *Dalton Trans.* **2007**, 37−40.

(24) Kamiyama, A.; Kajiwara, T.; Ito, T. Cage-Type Hexacopper(II) Complex Formed by Chloride Template. *Chem. Lett.* **2002**, *31*, 980−981.

(25) Rivera-Carrillo, M.; Chakraborty, I.; Mezei, G.; Webster, R. D.; Raptis, R. G. Tuning of the $[Cu_3(\mu\text{-O})]^{4+/5+}$ Redox Couple: Spectroscopic Evidence of Charge Delocalization in the Mixed-Valent $[Cu_3(\mu\text{-O})]^{5+}$ Species. *Inorg. Chem.* **2008**, *47*, 7644−7650.

(26) Rivera-Carrillo, M.; Chakraborty, I.; Raptis, R. G. Systematic Synthesis of a Metal Organic Framework Based on Triangular $Cu_3(\mu_3$-OH) Secondary Building Units: From a 0-D Complex to a 1-D Chain and a 3-D Lattice. *Cryst. Growth Des.* **2010**, *10*, 2606−2612.

(27) Casarin, M.; Cingolani, A.; Di Nicola, C.; Falcomer, D.; Monari, M.; Pandolfo, L.; Pettinari, C. The Different Supramolecular Arrangements of the Triangular $[Cu_3(\mu_3\text{-OH})(\mu\text{-pz})_3]^{2+}$ (pz = Pyrazolate) Secondary Building Units. Synthesis of a Coordination Polymer with Permanent Hexagonal Channels. *Cryst. Growth Des.* **2007**, *7*, 676−685.

(28) Shi, K.; Mathivathanan, L.; Boudalis, A. K.; Turek, P.; Chakraborty, I.; Raptis, R. G. Nitrite Reduction by Trinuclear Copper Pyrazolate Complexes: An Example of a Catalytic, Synthetic Polynuclear NO Releasing System. *Inorg. Chem.* **2019**, *58*, 7537−7544.

(29) Mezei, G.; Rivera-Carrillo, M.; Raptis, R. G. Effect of Copper-Substitution on the Structure and Nuclearity of Cu(II)-Pyrazolates: From Trinuclear to Tetra-, Hexa- and Polynuclear Complexes. *Inorg. Chim. Acta* **2004**, *357*, 3721−3732.
(30) Carlotto, S.; Casarin, M.; Lanza, A.; Nestola, F.; Pandolfo, L.; Pettinari, C.; Scatena, R. Reaction of Copper(II) Chloroacetate with Pyrazole. Synthesis of a One-Dimensional Coordination Polymer and Unexpected Dehydrochlorination Reaction. *Cryst. Growth Des.* **2015**, *15*, 5910−5918.
(31) Casarin, M.; Cingolani, A.; Di Nicola, C.; Falcomer, D.; Monari, M.; Pandolfo, L.; Pettinari, C. The Different Supramolecular Arrangements of the Triangular $[Cu_3(\mu_3\text{-}OH)(\mu\text{-}pz)_3]^{2+}$ (pz = Pyrazolate) Secondary Building Units. Synthesis of a Coordination Polymer with Permanent Hexagonal Channels. *Cryst. Growth Des.* **2007**, *7*, 676−685.
(32) Contaldi, S.; Di Nicola, C.; Garau, F.; Karabach, Y. Y.; Martins, L. M. D. R. S.; Monari, M.; Pandolfo, L.; Pettinari, C.; Pombeiro, A. J. L. New Coordination Polymers Based on the Triangular $[Cu_3(\mu_3\text{-}OH)(\mu\text{-}pz)_3]^{2+}$ Unit and Unsaturated Carboxylates. *Dalton Trans.* **2009**, 4928−4941.
(33) Mezei, G. Sulfate-Bridged Dimeric Trinuclear Copper(II)-Pyrazolate Complex with Three Different Terminal Ligands. *Acta Crystallogr.* **2016**, *E72*, 1064−1067.
(34) Zheng, L.-L.; Leng, J.-D.; Zheng, S.-L.; Zhaxi, Y.-C.; Zhang, W.-X.; Tong, M.-L. Engineering Delocalizing π Electronic $[Cu^{II}_3(\mu_3\text{-}OH)(\mu\text{-}pz)_3]^{2+}$ Species into Organometallic Frameworks by Ag-π Coordination. *CrystEngComm* **2008**, *10*, 1467−1473.
(35) Zhou, Q.-J.; Liu, Y.-Z.; Wang, R.-L.; Fu, J.-W.; Xu, J.-Y.; Lou, J.-S. Synthesis, Crystal Structure and Magnetic Properties of a Trinuclear Cu(II)-Pyrazolate Complex Containing μ_3-OH. *J. Coord. Chem.* **2009**, *62*, 311−318.
(36) Di Nicola, C.; Garau, F.; Gazzano, M.; Monari, M.; Pandolfo, L.; Pettinari, C.; Pettinari, R. Reactions of a Coordination Polymer Based on the Triangular Cluster $[Cu_3(\mu_3\text{-}OH)(\mu\text{-}pz)_3]^{2+}$ with Strong Acids. Crystal Structure and Supramolecular Assemblies of New Mono-, Tri-, and Hexanuclear Complexes and Coordination Polymers. *Cryst. Growth Des.* **2010**, *10*, 3120−3131.
(37) Sakai, K.; Yamada, Y.; Tsubomura, T.; Yabuki, M.; Yamaguchi, M. Synthesis, Crystal Structure, and Solution Properties of a Hexacopper(II) Complex with Bridging Hydroxides, Pyrazolates, and Nitrates. *Inorg. Chem.* **1996**, *35*, 542−544.
(38) Zhao, N.; Yang, L.; Pan, Q.; Han, J.; Li, X.; Liu, M.; Wang, Y.; Wang, X.; Pan, Q.; Zhu, G. Step-by-Step Assembly of Metal−Organic Frameworks from Trinuclear Cu_3 Clusters. *Inorg. Chem.* **2019**, *58*, 199−203.
(39) Gao, W.-Y.; Chen, Y.; Niu, Y.; Williams, K.; Cash, L.; Perez, P. J.; Wojtas, L.; Cai, J.; Chen, Y.-S.; Ma, S. Crystal Engineering of an nbo Topology Metal−Organic Framework for Chemical Fixation of CO_2 under Ambient Conditions. *Angew. Chem., Int. Ed.* **2014**, *53*, 2615−2619.
(40) Gao, W.-Y.; Pham, T.; Forrest, K. A.; Space, B.; Wojtas, L.; Chen, Y.-S.; Ma, S. The Local Electric Field Favours More than Exposed Nitrogen Atoms on CO_2 Capture: A Case Study on the rht-Type MOF Platform. *Chem. Commun.* **2015**, *51*, 9636−9639.
(41) Han, Y.; Liu, K.; Sinnwell, M. A.; Liu, L.; Huang, H.; Thallapally, P. K. Direct Observation of Li^+ Ions Trapped in a Mg^{2+}-Templated Metal−Organic Framework. *Inorg. Chem.* **2019**, *58*, 8922−8926.
(42) Bala, S.; Bhattacharya, S.; Goswami, A.; Adhikary, A.; Konar, S.; Mondal, R. Designing Functional Metal−Organic Frameworks by Imparting a Hexanuclear Copper-Based Secondary Building Unit Specific Properties: Structural Correlation With Magnetic and Photocatalytic Activity. *Cryst. Growth Des.* **2014**, *14*, 6391−6398.
(43) Akhtar, S.; Bala, S.; De, A.; Das, K. S.; Adhikary, A.; Jyotsna, S.; Poddar, P.; Mondal, R. Designing Multifunctional MOFs Using the Inorganic Motif $[Cu_3(\mu_3\text{-}OH)(\mu\text{-}Pyz)]$ as an SBU and Their Properties. *Cryst. Growth Des.* **2019**, *19*, 992−1004.
(44) Gao, W.-Y.; Cai, R.; Pham, T.; Forrest, K. A.; Hogan, A.; Nugent, P.; Williams, K.; Wojtas, L.; Luebke, R.; Weseliński, Ł. J.; Zaworotko, M. J.; Space, B.; Chen, Y.-S.; Eddaoudi, M.; Shi, X.; Ma, S. Remote Stabilization of Copper Paddlewheel Based Molecular Building Blocks in Metal−Organic Frameworks. *Chem. Mater.* **2015**, *27*, 2144−2151.
(45) Zhang, J.; Lu, Y.; Zhang, Z.-M.; Wang, E.-B. A Three-Dimensional Metal−Organic Framework Based on Hexanuclear Copper Units with Unsaturated Cu^{II} centers. *Inorg. Chem. Commun.* **2012**, *17*, 9−12.
(46) Liu, Q.; Song, Y.; Ma, Y.; Zhou, Y.; Cong, H.; Wang, C.; Wu, J.; Hu, G.; O'Keeffe, M.; Deng, H. Mesoporous Cages in Chemically Robust MOFs Created by a Large Number of Vertices with Reduced Connectivity. *J. Am. Chem. Soc.* **2019**, *141*, 488−496.
(47) Mathivathanan, L.; Torres-King, J.; Primera-Pedrozo, J. N.; García-Ricard, O. J.; Hernández-Maldonado, A. J.; Santana, J. A.; Raptis, R. G. Selective CO_2 Adsorption on Metal-Organic Frameworks Based on Trinuclear Cu_3-Pyrazolato Complexes: An Experimental and Computational Study. *Cryst. Growth Des.* **2013**, *13*, 2628−2635.
(48) Su, S.; Zhang, Y.; Zhu, M.; Song, X.; Wang, S.; Zhao, S.; Song, S.; Yang, X.; Zhang, H. An Active-Site-Accessible Porous Metal−Organic Framework Composed of Triangular Building Units: Preparation, Catalytic Activity and Magnetic Property. *Chem. Commun.* **2012**, *48*, 11118−11120.
(49) Di Nicola, C.; Forlin, E.; Garau, F.; Gazzano, M.; Lanza, A.; Monari, M.; Nestola, F.; Pandolfo, L.; Pettinari, C.; Zorzi, A.; Zorzi, F. Coordination Polymers Based on the Trinuclear Triangular Secondary Building Unit $[Cu_3(\mu_3\text{-}OH)(\mu\text{-}pz)_3]^{2+}$ (pz = pyrazolate) and Succinate Anion. *Cryst. Growth Des.* **2013**, *13*, 126−135.
(50) Condello, F.; Garau, F.; Lanza, A.; Monari, M.; Nestola, F.; Pandolfo, L.; Pettinari, C. Synthesis and Structural Characterizations of New Coordination Polymers Generated by the Interaction Between the Trinuclear Triangular SBU $[Cu_3(\mu_3\text{-}OH)(\mu\text{-}pz)_3]^{2+}$ and 4,4′-Bipyridine. *Cryst. Growth Des.* **2015**, *15*, 4854−4862.
(51) Zhang, T.; Lu, Y.; Zhang, Z.; Lan, Q.; Liu, D.; Wang, E. Single-Crystal to Single-Crystal Transformation from a Hydrophilic−Hydrophobic Metal−Organic Framework to a Layered Coordination Polymer. *Inorg. Chim. Acta* **2014**, *411*, 128−133.
(52) Casarin, M.; Corvaja, C.; Di Nicola, C.; Falcomer, D.; Franco, L.; Monari, M.; Pandolfo, L.; Pettinari, C.; Piccinelli, F. One-Dimensional and Two-Dimensional Coordination Polymers from Self-Assembling of Trinuclear Triangular Cu(II) Secondary Building Units. *Inorg. Chem.* **2005**, *44*, 6265−6276.
(53) Kreiger, D. I.; Mathivathanan, L.; Raptis, R. G. Coordination Polymers Based on Pyrazole-4-Carboxaldehyde-Containing Cu_3N_6 Metallacycles as Building Units. *CrystEngComm* **2019**, *21*, 3047−3055.
(54) Di Nicola, C.; Garau, F.; Gazzano, M.; Guedes da Silva, M. F. C.; Lanza, A.; Monari, M.; Nestola, F.; Pandolfo, L.; Pettinari, C.; Pombeiro, A. J. L. New Coordination Polymers and Porous Supramolecular Metal Organic Network Based on the Trinuclear Triangular Secondary Building Unit $[Cu_3(\mu_3\text{-}OH)(\mu\text{-}pz)_3]^{2+}$ and 4,4′-Bipyridine. *Cryst. Growth Des.* **2012**, *12*, 2890−2901.
(55) Shi, K.; Mathivathanan, L.; Herchel, R.; Boudalis, A. K.; Raptis, R. G. Supramolecular Assemblies of Trinuclear Copper(II)-Pyrazolato Units: A Structural, Magnetic and EPR Study. *Chemistry* **2020**, *2*, 626−644.
(56) Shi, K.; Mathivathanan, L.; Drozd, V. A.; Raptis, R. G. Three Topological Isomers of 1D- and 2D-Coordination Polymers Consisting of Tricopper Pyrazolate SBUs and 4,4′-Trimethylenedipyridine Linkers: Effect of Pressure on the Structure. *Cryst. Growth Des.* **2019**, *19*, 381−390.
(57) Wang, P.; Hou, Q.-Q.; Cui, X.-L.; You, G.-D. Development of Two Cu(II) and Cd(II) Coordination Complexes Based on Mixed-Ligand Approach and Application of their Nanostructures as Potential Anti-Breast Cancer Agents. *J. Mol. Struct.* **2019**, *1193*, 62−68.
(58) Di Nicola, C.; Garau, F.; Gazzano, M.; Lanza, A.; Monari, M.; Nestola, F.; Pandolfo, L.; Pettinari, C. Interaction of the Trinuclear Triangular Secondary Building Unit $[Cu_3(\mu_3\text{-}OH)(\mu\text{-}pz)_3]^{2+}$ with 4,4′-Bipyridine. Structural Characterizations of New Coordination

https://doi.org/10.1021/acs.inorgchem.1c01826
Inorg. Chem. 2021, 60, 13479−13492

Polymers and Hexanuclear Cu^{II} Clusters. *Cryst. Growth Des.* **2015**, *15*, 1259−1272.
(59) Forlin, E.; Lanza, A.; Di Nicola, C.; Monari, M.; Gazzano, M.; Nestola, F.; Pettinari, C.; Pandolfo, L. 1D and 3D Coordination Polymers based on the $Cu_3(\mu_3\text{-OH})(\mu\text{-pz})_3$ and $Cu(Hpz)_3$ SBUs Connected by the Flexible Glutarate Dianion. *Inorg. Chim. Acta* **2018**, *470*, 385−392.
(60) Di Nicola, C.; Forlin, E.; Garau, F.; Lanza, A.; Natile, M. M.; Nestola, F.; Pandolfo, L.; Pettinari, C. Coordination Polymers Based on Trinuclear and Mononuclear Copper-Pyrazolate Building Moieties Connected by Fumarate or 2-Methylfumarate Ions. *J. Organomet. Chem.* **2012**, *714*, 74−80.
(61) Halcrow, M. A. Pyrazoles and Pyrazolides—Flexible Synthons in Self-Assembly. *Dalton Trans.* **2009**, 2059−2073.
(62) Viciano-Chumillas, M.; Tanase, S.; de Jongh, L. J.; Reedijk, J. Coordination Versatility of Pyrazole-Based Ligands towards High-Nuclearity Transition-Metal and Rare-Earth Clusters. *Eur. J. Inorg. Chem.* **2010**, *2010*, 3403−3418.
(63) Santra, B.; Kalita, P.; Chandra, S.; Mandal, D.; Kumar, V.; Narayanan, R. S.; Dey, A.; Chrysochos, N.; Huch, V.; Biswas, S.; Ghoshal, D.; Sañudo, E. C.; Sarkar, B.; Schulzke, C.; Chandrasekhar, V.; Jana, A. Molecular Enneanuclear Cu^{II} Phosphates Containing Planar Hexanuclear and Trinuclear Sub-Units: Syntheses, Structures, and Magnetism. *Dalton Trans.* **2020**, *49*, 2527−2536.
(64) Li, H.-X.; Ren, Z.-G.; Liu, D.; Chen, Y.; Lang, J.-P.; Cheng, Z.-P.; Zhu, X.-L.; Abrahams, B. F. Single-Crystal-to-Single-Crystal Structural Transformations of Two Sandwich-Like Cu(II) Pyrazolate Complexes and their Excellent Catalytic Performances in MMA Polymerization. *Chem. Commun.* **2010**, *46*, 8430−8432.
(65) Sheikh, J. A.; Jena, H. S.; Adhikary, A.; Khatua, S.; Konar, S. An Unprecedented Octadecanuclear Copper(II) Pyrazolate−Phosphonate Nanocage: Synthetic, Structural, Magnetic, and Mechanistic Study. *Inorg. Chem.* **2013**, *52*, 9717−9719.
(66) Denisova, T. O.; Amel'chenkova, E. V.; Pruss, I. V.; Dobrokhotova, Z. V.; Fialkovskii, O. P.; Nefedov, S. E. Copper(II) Trimethylacetate Complexes with 3,5-Dimethylpyrazole. *Russ. J. Inorg. Chem.* **2006**, *51*, 1020−1064.
(67) Xu, Y.; Xia, P.; Wang, X.; Wei, W.; Zhang, F.; Hu, C. Positional Disorder of Cu(II) Ions in a Cluster: A Novel Heptanuclear Cu(II) Core Supported by 4-Bromo-3,5-Dimethylpyrazolate. *CrystEngComm* **2011**, *13*, 2820−2823.
(68) Mohamed, A. A.; Ricci, S.; Burini, A.; Galassi, R.; Santini, C.; Chiarella, G. M.; Melgarejo, D. Y.; Fackler, J. P., Jr. Halide and Nitrite Recognizing Hexanuclear Metallacycle Copper(II) Pyrazolates. *Inorg. Chem.* **2011**, *50*, 1014−1020.
(69) Cañon-Mancisidor, W.; Gómez-García, C. J.; Espallargas, G. M.; Vega, A.; Spodine, E.; Venegas-Yazigi, D.; Coronado, E. Structural Re-arrangement in Two Hexanuclear Cu^{II} Complexes: From a Spin Frustrated Trigonal Prism to a Strongly Coupled Antiferromagnetic Soluble Ring Complex with a Porous Tubular Structure. *Chem. Sci.* **2014**, *5*, 324−332.
(70) Govor, E. V.; Lysenko, A. B.; Quiñonero, D.; Rusanov, E. B.; Chernega, A. N.; Moellmer, J.; Staudt, R.; Krautscheid, H.; Frontera, A.; Domasevitch, K. V. Self-Assembly Hexanuclear Metallacontainer Hosting Halogenated Guest Species and Sustaining Structure of 3D Coordination Framework. *Chem. Commun.* **2011**, *47*, 1764−1766.
(71) Dodds, C. A.; Kennedy, A. R. Formation of a Nonanuclear Copper(II) Cluster with 3,5-Dimethylpyrazolate Starting from an NHC Complex of Copper(I) Chloride. *Acta Crystallogr.* **2020**, *E76*, 1486−1490.
(72) Yu, F.; Ji, B.-Q.; Jagodič, M.; Su, Y.-M.; Zhang, S.-S.; Feng, L.; Kurmoo, M.; Jagličić, Z.; Sun, D. Copper(II)-Assisted Ligand Fragmentation Leading to Three Families of Metallamacrocycle. *Inorg. Chem.* **2020**, *59*, 13524−13532.
(73) Massignani, S.; Scatena, R.; Lanza, A.; Monari, M.; Condello, F.; Nestola, F.; Pettinari, C.; Zorzi, F.; Pandolfo, L. Coordination Polymers from Mild Condition Reactions of Copper(II) Carboxylates with Pyrazole (Hpz). Influence of Carboxylate Basicity on the Self-Assembly of the $[Cu_3(\mu_3\text{-OH})(\mu\text{-pz})_3]^{2+}$ Secondary Building Unit. *Inorg. Chim. Acta* **2017**, *455*, 618−626.
(74) Mathivathanan, L.; Rivera-Carrillo, M.; Raptis, R. G. Three New Multinuclear Motifs in Cu(II)-Pyrazolate Chemistry. *Inorg. Chim. Acta* **2012**, *391*, 201−205.
(75) Fernando, I. R.; Surmann, S. A.; Urech, A. A.; Poulsen, A. M.; Mezei, G. Selective Total Encapsulation of the Sulfate Anion by Neutral Nano-Jars. *Chem. Commun.* **2012**, *48*, 6860−6862.
(76) Ahmed, B. M.; Szymczyna, B. R.; Jianrattanasawat, S.; Surmann, S. A.; Mezei, G. Survival of the Fittest Nanojar: Stepwise Breakdown of Polydisperse Cu_{27}−Cu_{31} Nanojar Mixtures into Monodisperse $Cu_{27}(CO_3)$ and $Cu_{31}(SO_4)$ Nanojars. *Chem. - Eur. J.* **2016**, *22*, 5499−5503.
(77) Ahmed, B. M.; Hartman, C. K.; Mezei, G. Sulfate-Incarcerating Nanojars: Solution and Solid-State Studies, Sulfate Extraction from Water, and Anion Exchange with Carbonate. *Inorg. Chem.* **2016**, *55*, 10666−10679.
(78) Mezei, G. Incarceration of One or Two Phosphate or Arsenate Species within Nanojars, Capped Nanojars and Nanohelicages: Helical Chirality from Two Closely-Spaced, Head-to-Head PO_4^{3-} or AsO_4^{3-} Ions. *Chem. Commun.* **2015**, *51*, 10341−10344.
(79) Ahmed, B. M.; Calco, B.; Mezei, G. Tuning the Structure and Solubility of Nanojars by Peripheral Ligand Substitution, Leading to Unprecedented Liquid−Liquid Extraction of the Carbonate Ion from Water into Aliphatic Solvents. *Dalton Trans.* **2016**, *45*, 8327−8339.
(80) Mezei, G. Selective Extraction of Anions from Solutions. U.S. Patent 9,901,901 B2, Feb 27, 2018, U.S. Patent 10,087,197 B2, Oct 2, 2018, European Patent 2852558 B1, Sept 9, 2020.
(81) Chen, L.; Berry, S. N.; Wu, X.; Howe, E. N. W.; Gale, P. A. Advances in Anion Receptor Chemistry. *Chem.* **2020**, *6*, 61−141.
(82) Liu, Y.; Sengupta, A.; Raghavachari, K.; Flood, A. H. Anion Binding in Solution: Beyond the Electrostatic Regime. *Chem.* **2017**, *3*, 411−427.
(83) Molina, P.; Zapata, F.; Caballero, A. Anion Recognition Strategies Based on Combined Noncovalent Interactions. *Chem. Rev.* **2017**, *117*, 9907−9972.
(84) Busschaert, N.; Caltagirone, C.; Van Rossom, W.; Gale, P. A. Applications of Supramolecular Anion Recognition. *Chem. Rev.* **2015**, *115*, 8038−8155.
(85) Mezei, G.; Baran, P.; Raptis, R. G. Anion Encapsulation by Neutral Supramolecular Assemblies of Cyclic Cu^{II} Complexes: A Series of Five Polymerization Isomers, $[\{cis\text{-}Cu^{II}(\mu\text{-OH})(\mu\text{-pz})\}_n]$, n = 6, 8, 9, 12, and 14. *Angew. Chem., Int. Ed.* **2004**, *43*, 574−577.
(86) Ahmed, B. M.; Mezei, G. From Ordinary to Extraordinary: Insights into the Formation Mechanism and pH-Dependent Assembly/Disassembly of Nanojars. *Inorg. Chem.* **2016**, *55*, 7717−7728.
(87) Mezei, G. Reversible CO_2 Sequestration by Precipitation from Water via an Organic Sorbent. *Chem.* **2019**, *5*, 499−501. and references cited therein
(88) Gutmann, V. *The Donor−Acceptor Approach to Molecular Interactions*, 1st ed.; Springer USA, 1978.
(89) Alder, C. M.; Hayler, J. D.; Henderson, R. K.; Redman, A. M.; Shukla, L.; Shuster, L. E.; Sneddon, H. F. Updating and Further Expanding GSK's Solvent Sustainability Guide. *Green Chem.* **2016**, *18*, 3879−3890.
(90) Tshepelevitsh, S.; Kütt, A.; Lõkov, M.; Kaljurand, I.; Saame, J.; Heering, A.; Plieger, P. G.; Vianello, R.; Leito, I. On the Basicity of Organic Bases in Different Media. *Eur. J. Org. Chem.* **2019**, *2019*, 6735−6748.
(91) *SAINT*, version 8.38A; Bruker: Madison, WI, 2017.
(92) Krause, L.; Herbst-Irmer, R.; Sheldrick, G. M.; Stalke, D. Comparison of Silver and Molybdenum Microfocus X-Ray Sources for Single-Crystal Structure Determination. *J. Appl. Crystallogr.* **2015**, *48*, 3−10.
(93) Sheldrick, G. M. A Short History of *SHELX*. *Acta Crystallogr., Sect. A: Found. Crystallogr.* **2008**, *A64*, 112−122.
(94) Sheldrick, G. M. Crystal Structure Refinement with *SHELXL*. *Acta Crystallogr., Sect. C: Struct. Chem.* **2015**, *C71*, 3−8.

https://doi.org/10.1021/acs.inorgchem.1c01826
Inorg. Chem. 2021, 60, 13479−13492